

RESEARCH ARTICLE SUMMARY

IMAGING

Whole-body magnetic resonance imaging at 0.05 Tesla

Yujiao Zhao, Ye Ding, Vick Lau, Christopher Man, Shi Su, Linfang Xiao, Alex T. L. Leong, Ed X. Wu*

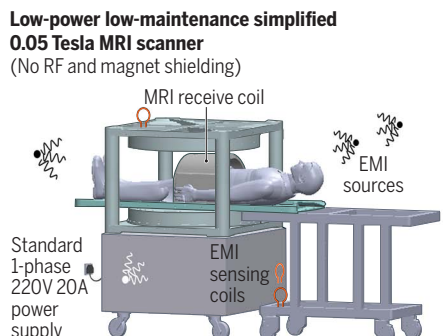
INTRODUCTION: Magnetic resonance imaging (MRI) has revolutionized healthcare with its nonionizing, noninvasive, multicontrast, and quantitative capabilities. It also presents a promising platform for future artificial intelligence-driven medical diagnoses. However, after five decades of development, MRI accessibility—especially in low and middle-income countries—remains low and highly uneven due to high costs and specialized settings required for standard superconducting MRI scanners. These scanners are mostly found in specialized radiology departments and large imaging centers, restricting their availability in other medical settings. The need for radio frequency (RF)-shielded rooms and high power consumption further adds to hardware cost and compromises mobility and patient-friendliness.

RATIONALE: We developed a highly simplified whole-body ultra-low-field (ULF) MRI scanner that operates on a standard wall power outlet without RF or magnetic shielding cages. This scanner uses a compact 0.05 Tesla permanent magnet and incorporates active sensing and deep learning to address electromagnetic interference (EMI) signals. We deployed EMI sensing coils positioned around the scanner and implemented a deep learning method to directly predict EMI-free nuclear magnetic resonance signals from acquired data. To enhance image quality and reduce scan time, we also developed a data-driven deep learning image formation method, which integrates image reconstruction and three-dimensional (3D) multiscale super-resolution and leverages the homogeneous human anatomy and image

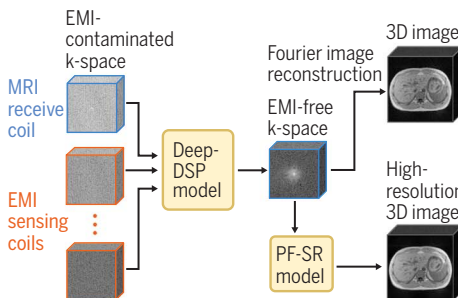
contrasts available in large-scale, high-field, high-resolution MRI data.

RESULTS: We implemented commonly used clinical protocols at 0.05 Tesla, including T1-weighted, T2-weighted, and diffusion-weighted imaging, and optimized their contrasts for different anatomical structures. Each protocol was designed to have a scan time of 8 minutes or less with an image resolution of approximately $2 \times 2 \times 8 \text{ mm}^3$. The scanner power consumption during scanning was under 1800W and around 300W when idle. We conducted imaging on healthy volunteers, capturing brain, spine, abdomen, lung, musculoskeletal, and cardiac images. Deep learning signal prediction effectively eliminated EMI signals, enabling clear imaging without shielding. The brain images showed various brain tissues whereas the spine images revealed intervertebral disks, spinal cord, and cerebrospinal fluid. Abdominal images displayed major structures like the liver, kidneys, and spleen. Lung images showed pulmonary vessels and parenchyma. Knee images identified knee structures such as cartilage and meniscus. Cardiac cine images depicted the left ventricle contraction and neck angiography revealed carotid arteries. Furthermore, deep learning image formation greatly improved the 0.05 Tesla image quality for various anatomical structures, including the brain, spine, abdomen, and knee; it also effectively suppressed noise and artifacts and increased image spatial resolution.

CONCLUSION: To address MRI accessibility challenges, we developed a low-power and simplified whole-body 0.05 Tesla MRI scanner that operates without the need for RF or magnetic shielding and that can be manufactured, maintained, and operated at a low cost. We experimentally demonstrated the general utility of this scanner for imaging various human anatomical structures at a whole-body level, even in the presence of strong EMI signals, with acceptable scan time. Moreover, we demonstrated the potential of deep learning image formation to substantially augment 0.05 Tesla image quality by exploiting computing and extensive high-field MRI data. These advances pave the way for affordable, patient-centric, and deep learning-powered ULF MRI scanners, addressing unmet clinical needs in diverse healthcare settings worldwide. ■



Deep learning EMI elimination and image formation



Multi-contrast images using Fourier reconstruction



High-resolution multi-contrast images using data-driven PF-SR image formation



Computing-powered whole-body MRI at 0.05 Tesla. (Top) Prototype of a low-cost, low-power, compact, and shielding-free imaging system using an open 0.05 Tesla permanent magnet. It incorporates active sensing and deep learning to address EMI signals. (Middle) Typical images of various anatomical structures using conventional image reconstruction. (Bottom) High-resolution images using deep learning image formation by harnessing large-scale high-field MRI data.

The list of author affiliations is available in the full article.

*Corresponding author. Email: ewu@eee.hku.hk

Cite this article as Y. Zhao et al., *Science* **384**, eadm7168 (2024). DOI: 10.1126/science.adm7168

S READ THE FULL ARTICLE AT
<https://doi.org/10.1126/science.adm7168>

RESEARCH ARTICLE

IMAGING

Whole-body magnetic resonance imaging at 0.05 Tesla

Yujiao Zhao^{1,2}, Ye Ding^{1,2}, Vick Lau^{1,2}, Christopher Man^{1,2}, Shi Su^{1,2}, Linfang Xiao^{1,2}, Alex T. L. Leong^{1,2}, Ed X. Wu^{1,2*}

Despite a half-century of advancements, global magnetic resonance imaging (MRI) accessibility remains limited and uneven, hindering its full potential in health care. Initially, MRI development focused on low fields around 0.05 Tesla, but progress halted after the introduction of the 1.5 Tesla whole-body superconducting scanner in 1983. Using a permanent 0.05 Tesla magnet and deep learning for electromagnetic interference elimination, we developed a whole-body scanner that operates using a standard wall power outlet and without radiofrequency and magnetic shielding. We demonstrated its wide-ranging applicability for imaging various anatomical structures. Furthermore, we developed three-dimensional deep learning reconstruction to boost image quality by harnessing extensive high-field MRI data. These advances pave the way for affordable deep learning-powered ultra-low-field MRI scanners, addressing unmet clinical needs in diverse health care settings worldwide.

The seminal development of magnetic resonance imaging (MRI) by Paul C. Lauterbur and Sir Peter Mansfield five decades ago revolutionized modern medicine (1, 2). MRI is now widely regarded as one of the most important inventions for health care (3). Over 150 million MRI examinations are performed worldwide each year (4), with applications including diagnosing and prognosis diseases such as tumors and strokes, evaluating injuries in the nervous, hepatobiliary, pancreatic, and musculoskeletal systems, and guidance of interventional procedures. MRI holds inherent advantages over other imaging modalities; specifically, it is non-ionizing, non-invasive, inherently three-dimensional (3D), quantitative, and multiparametric (5). These qualities not only make MRI superior to other imaging modalities but also position it as a promising platform for future artificial intelligence-driven medical diagnoses.

Nonetheless, MRI accessibility remains low and highly uneven worldwide. As per the statistics provided by the 2022 Organisation for Economic Co-operation and Development, there are around 70,000 MRI scanner installations across the globe (6). The distribution of these scanners is primarily concentrated in developed nations, with limited availability in low and middle-income countries. For instance, Africa has a mere 0.7 MRI scanners per million residents (7), in stark contrast to the US and Japan, which have 40 and 55 scanners per million inhabitants, respectively, presenting an exemplary case of ever-expanding

global health care disparity (8). This scenario primarily stems from the considerable costs associated with the procurement, installation, maintenance, and operation of existing standard high-field superconducting MRI scanners (1.5 T and 3 T). These clinical MRI scanners are predominantly located in highly specialized radiology departments, large centralized imaging centers, and often situated on the ground floors of hospitals and clinics with magnetic shielding. As a result, MRI scanners are mostly unavailable in trauma centers, acute care facilities, surgery suites, pediatric clinics, and community clinics even in developed countries. Moreover, these scanners prevent external electromagnetic interference (EMI) through the passive use of bulky and fully enclosed radio frequency (RF)-shielded rooms, thus posing further hardware costs and compromising their mobility and patient-friendliness.

Recently, there have been intensive efforts to develop low-cost MRI scanners for brain imaging at ultra-low-field (ULF) strengths (<0.1 T) (9–14). Studies have shown that key neuroimaging protocols can be successfully implemented on ULF scanners, providing valuable information for diagnosing brain lesions resulting from tumor and stroke, for example (12, 15, 16). The need for RF-shielded rooms is also being challenged by active detection and retrospective removal of environmental EMI signals using analytical and deep learning approaches (12, 17, 18), offering the promise of shielding-free and thus portable and more patient-friendly MRI. Recent studies have highlighted the potential of such brain ULF scanners for point-of-care applications in intensive care units and COVID-19 wards (15, 16, 19). Concurrently, deep learning advances offer exceptional capabilities for multidimensional

feature extraction (20, 21), presenting approaches to address the low magnetic resonance (MR) signal-to-noise ratio (SNR) inherent to ULF. For example, deep learning super-resolution strategies have been recently pursued for brain ULF MRI to suppress image noise and boost resolution by leveraging the homogeneous brain structures and image contrasts available in human brain high-field MRI data (22, 23). However, these developments have been confined to imaging of the brain (9–14) and extremities (24). To fully harness the potential of ULF MRI for accessible health care, it is imperative to develop ULF MRI technologies, including deep learning techniques, for imaging all organs at the whole-body level.

In this study, we present the development of a low-cost, low-power, and computing-driven shielding-free ULF MRI scanner for whole-body imaging. It features a homogeneous 0.05 T permanent magnet and linear imaging gradients, enabling us to implement ULF MRI protocols by building upon the methodologies developed for high-field MRI over the past five decades. To achieve robust EMI elimination for shielding-free scanning, we deployed a method to directly predict EMI-free MR signals through deep learning (25). We demonstrated the wide-ranging applicability of this scanner for imaging various anatomical structures, including the brain, spine, abdomen, heart, lungs, and extremities. Furthermore, we demonstrated the promise of deep learning 3D image formation on this whole-body ULF MRI platform by learning from large-scale high-field MRI data, using a method we developed (26).

Results

Shielding-free 0.05 Tesla whole-body MRI scanner design

We demonstrated the feasibility of cost-effective MRI technology by designing and prototyping a whole-body MRI scanner that operates on a standard alternating current (AC) wall power outlet (single-phase 220V 20A) without any RF or magnetic shielding cages (Fig. 1). The system utilized a compact 0.05 T permanent neodymium ferrite boron (NdFeB) magnet with a double-plate structure (Fig. 1A). Key magnet components included yokes, NdFeB plates, poles, anti-eddy current plates, and shimming rings (Fig. 1B). It generated a 0.05 T field with inhomogeneity <10,000 parts per million (ppm) peak-to-peak over an oblate ellipsoid volume of diameter 40 cm and height 38 cm. After passive shimming, this inhomogeneity was reduced to <200 ppm peak-to-peak. The 5 Gauss fringe field was small, within 104 cm, 114 cm, and 104 cm in the X, Y, and Z directions, respectively, from the magnet center. We used standard and low-cost off-the-shelf electronics for simplicity, including a console and gradient amplifier. For quantity production, we estimate its hardware material costs to be ~USD

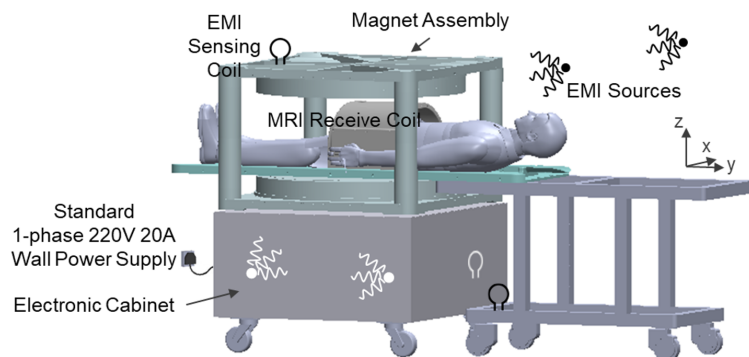
*Laboratory of Biomedical Imaging and Signal Processing, The University of Hong Kong, Pokfulam, Hong Kong SAR, China.

²Department of Electrical and Electronic Engineering, The University of Hong Kong, Pokfulam, Hong Kong SAR, China.

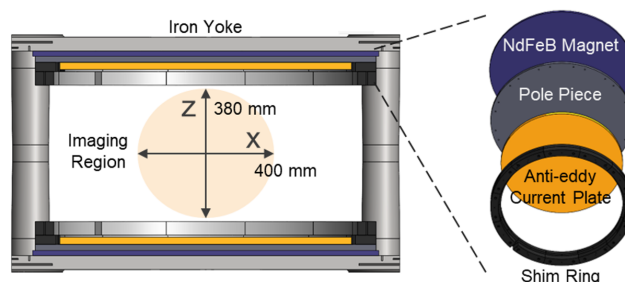
*Corresponding author. Email: ewu@eee.hku.hk

A

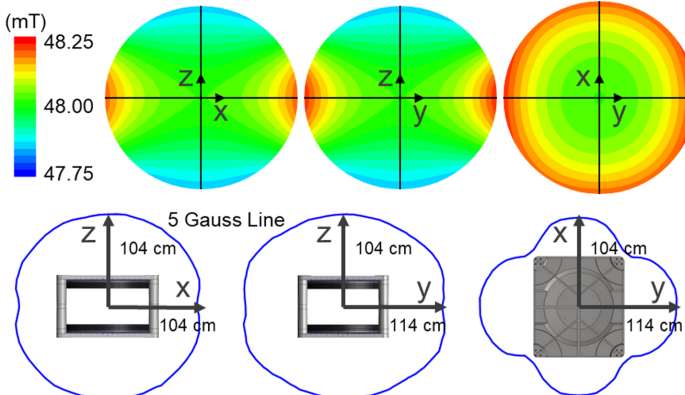
0.05 Tesla Shielding-free Whole-body MRI System

**B**

Cross-section of Magnet & Magnet Components



Field Homogeneity Map & Fringe Field of Magnet

**Fig. 1. Prototype of a low-cost, low-power, and shielding-free whole-body****ULF MRI scanner with a homogeneous 0.05 Tesla NdFeB magnet and small**

5 Gauss fringe field. (A) The scanner is designed to operate solely on a standard AC wall power outlet. It incorporates 10 small EMI sensing coils to actively detect EMI signal during scanning, has a compact footprint of $\sim 1.3 \text{ m}^2$ (excluding the detachable patient bed), and requires neither magnetic nor RF shielding cages. (B) The magnet assembly includes iron yokes, pillars, NdFeB plates, poles, anti-eddy current plates, and shimming rings, with a vertical gap of 40 cm and a width of 92 cm. It has a homogeneity of $<200 \text{ ppm}$ peak-to-peak over a 40 cm diameter and 38 cm height oblate ellipsoid volume, and weighs $\sim 1300 \text{ kg}$.

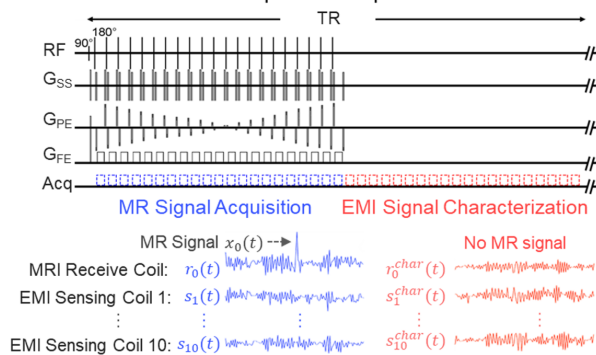
22K mainly for the magnet, gradient and RF, and console subsystems (table S1).

The scanner required no RF shielding cages. To robustly address the EMI from both external environments and internal low-cost electronics during scanning, we deployed active sensing and deep learning to directly predict EMI-free MR signals. Ten small EMI sensing

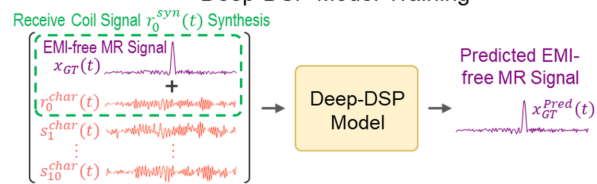
coils were positioned around the scanner and inside the electronic cabinet to simultaneously acquire radiative EMI signals during scanning (Fig. 1A). We developed and implemented a method termed deep learning direct signal prediction (Deep-DSP) (25) (Fig. 1C and fig. S1). In brief, both the MRI receive coil and EMI sensing coils sampled data within two

C

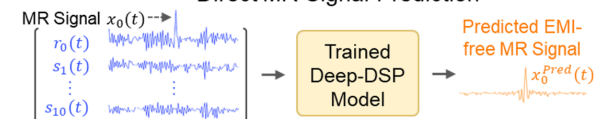
Data Acquisition Implementation



Deep-DSP Model Training



Direct MR Signal Prediction



(C) The scanner uses active EMI sensing and a deep learning Deep-DSP method to retrospectively eliminate EMI in MR k-space data by directly predicting EMI-free MR signals. A 3D FSE sequence is illustrated with MR signal collection and EMI signal characterization windows. Following each scan, data collected during the EMI characterization window, along with synthetic EMI-contaminated MRI data and EMI sensing coil data acquired during the EMI signal characterization window, were used to train a Deep-DSP model. This model was subsequently applied to predict EMI-free MR data using data acquired during the MR signal acquisition window. Note that the EMI signal characterization window is not always necessary because the outer k-space data collected during MR signal acquisition window may be used for training.

windows: one for MR signal acquisition and the other for EMI signal characterization data acquisition. No MR signal was present during the EMI signal characterization window. Using the synthetic EMI-contaminated MRI data and EMI sensing coil data acquired during the EMI signal characterization window, a residual U-Net model was trained to predict EMI-free

MR signal from signals acquired by both types of coils. The trained model was then used to predict EMI-free MR signal from data acquired during the MR signal acquisition window. This Deep-DSP strategy has been shown to yield superior performance (25) compared with all existing EMI reduction methods recently developed for brain ULF MRI (12, 17, 18). It is worth noting that, in practice, the EMI signal characterization window is not an absolute requirement for Deep-DSP (25).

Whole-body imaging at 0.05 Tesla

Over the past few decades, extensive research in high-field superconducting MRI has resulted in the development of a wide range of MRI contrasts and clinical protocols that enable the investigation of various organ structures and physiological abnormalities associated with different pathologies (27). The most commonly used MRI protocols are predominately based on the T1-weighted (T1W), T2-weighted (T2W), and diffusion-weighted (DW) contrasts. They are often acquired with gradient-recalled-echo (GRE), fast-spin-echo (FSE), balanced steady-state free procession (bSSFP), or echo-planar-imaging (EPI) pulse sequences. We implemented these imaging sequences, as well as the 3D stack-of-star (SoS) (28) radial sampling that

is less sensitive to respiratory body motions, by careful calibration of hardware imperfections, such as field inhomogeneity and gradient eddy currents/delays. We optimized their contrasts for the brain, spine, abdomen, heart, lungs, and extremities using phantoms and volunteers. For each protocol, scan time was kept at 8 min or less. In general, image resolution was set to be $\sim 2 \times 2 \times 8 \text{ mm}^3$ ($\sim 2\text{-mm}$ in-plane resolution and 8-mm slice thickness) by acquisition and $1 \times 1 \times 4 \text{ mm}^3$ by reconstruction for display, unless stated otherwise. Image reconstruction was performed here using traditional Fourier transform-based methods, including filtered backprojection reconstruction. All protocol details for various anatomical structures and contrasts are summarized in table S2. The total AC power consumption was under 1800W while scanning for all protocols and around 300W when not scanning.

We performed 0.05 T imaging in 30 healthy volunteers (23 to 77 years old). Typical brain axial T1W, T2W, FLAIR-like, and DWI images are shown in Fig. 2A, delineating various brain tissues such as gray matter, white matter, and cerebrospinal fluid (CSF). They were acquired with cartesian 3D GRE, long-TR 3D FSE, short-TR 3D FSE, and 2D EPI DWI sequences, respectively. Fig. 2, B and C, shows the typical

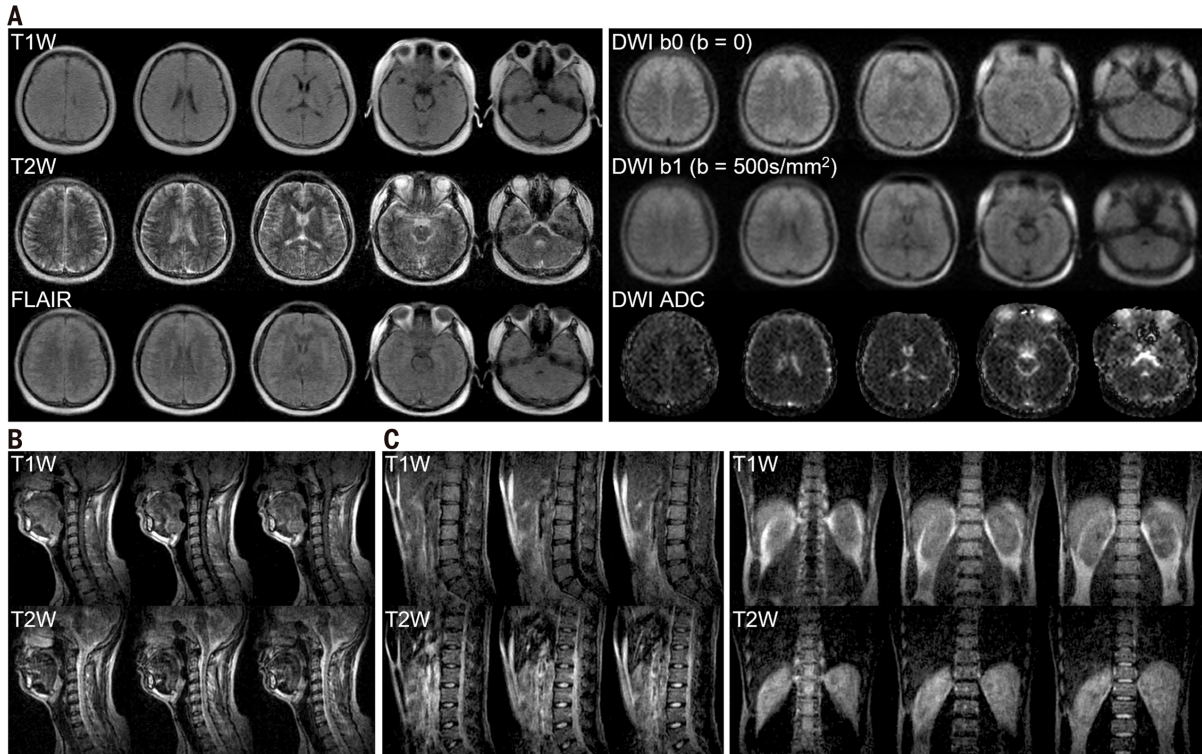
T1W and T2W C- and L-spine results. They were all acquired with cartesian 3D FSE sequences. Intervertebral disk and body, together with spinal cord and CSF inside the spinal canal, can be identified. Figure S2 displays the brain and spine images from Fig. 2 with and without EMI elimination. Deep-DSP fully removed EMI signals. Without Deep-DSP, image contents were completely obscured by EMI signals. Moreover, recently developed EMI removal methods, deep learning convolutional neural network (CNN) (12, 18), and analytical external dynamic interference estimation and removal (EDITER) (17), failed to effectively remove these intense EMI signals. These results demonstrated the robust ability of Deep-DSP in suppressing very strong EMI signals and enabling shielding-free 0.05 T whole-body imaging.

Figure 3, A and B, displays the typical abdominal T1W, T2W, and DWI images, which were acquired using free-breathing 3D SoS GRE, 3D SoS FSE, and cartesian 2D EPI DWI sequences, respectively. Major abdominal structures such as the liver, large hepatic vessels, kidneys, spleen, pancreas, stomach, spine, and muscle as well as subcutaneous and visceral fat can be readily seen in these images. Figure 3C shows the abdominal 3D bSSFP images. The contrast of these bSSFP images varied greatly

Fig. 2. Typical brain and spine images from healthy adults produced by the shielding-free whole-body 0.05 T MRI scanner.

(A) Axial brain T1W, T2W, FLAIR, and DWI images from a healthy volunteer (23 years old; male) using 3D GRE (TR/TE/ α = 48 ms/6.6 ms/40°; resolution $2 \times 2 \times 8 \text{ mm}^3$), long-TR 3D FSE (TR/TE/ETL = 1500 ms/200 ms/21), short-TR 3D FSE (TR/TE/ETL = 500 ms/127 ms/13), and 2D EPI DWI (TR/TE = 1400 ms/104 ms), respectively.

(B) Sagittal C-spine T1W and T2W images from a healthy volunteer (28 years old; male) using 3D FSE with TR/TE/ETL = 210 ms/76 ms/9 and 2300 ms/136 ms/25, respectively. (C) Coronal and sagittal L-spine images acquired using 3D FSE sequences (27 years old; male). Coronal T1W and T2W images were acquired with TR/TE/ETL = 190 ms/57 ms/7 and 1800 ms/170 ms/27,



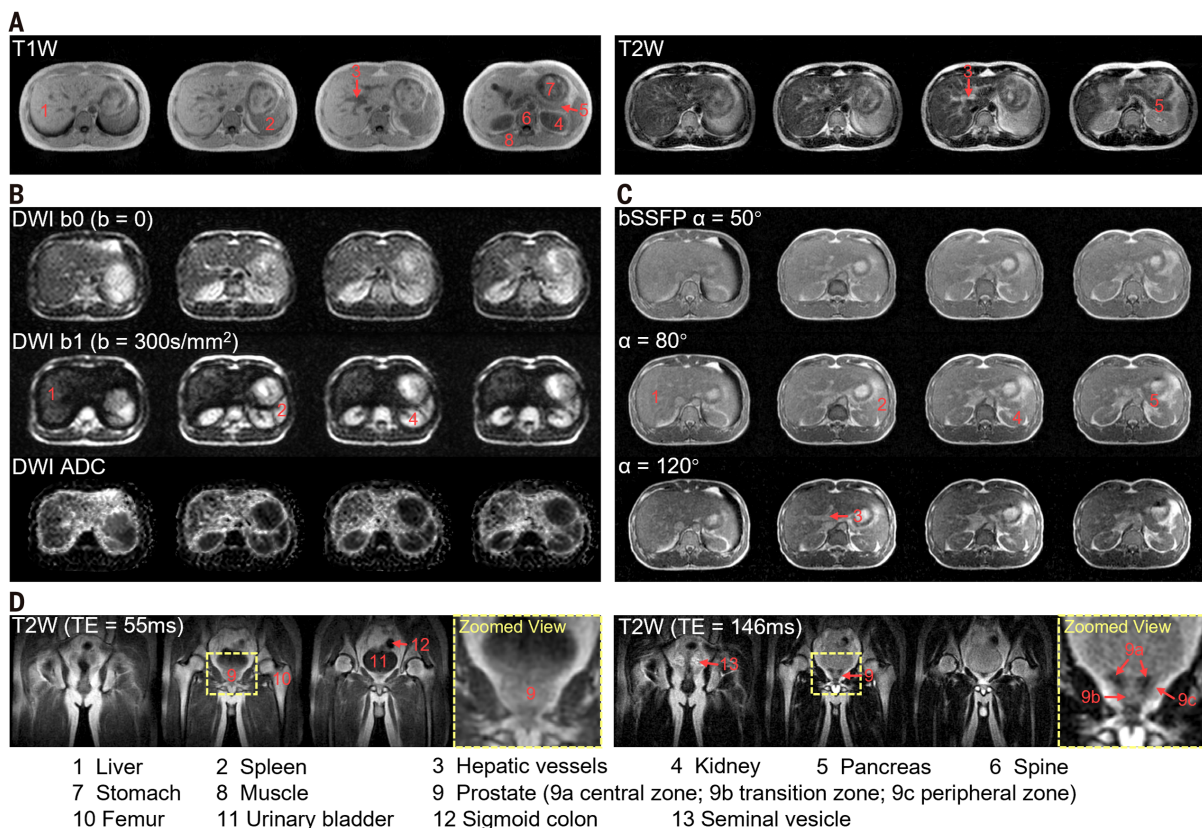
respectively. Sagittal T1W and T2W images were acquired with TR/TE/ETL = 190 ms/63 ms/7 and 1800 ms/172 ms/31, respectively. For each imaging protocol, scan time was 8 min or less. Image resolution was $\sim 2 \times 2 \times 8 \text{ mm}^3$ by acquisition and $1 \times 1 \times 4 \text{ mm}^3$ by reconstruction for display. See table S2 for protocol details.

with the flip angle, as expected, and image SNR was relatively high because the intrinsic bSSFP signal is mainly related to T2/T1 while tissue T1 relaxation times are generally much shorter at ULF (12, 29, 30). Figure 3D displays the typical pelvis coronal TIW and T2W images from a young male volunteer, in which normal prostate substructures can be distinguished.

Fig. 3. Typical abdominal and pelvic images from healthy adults produced by the shielding-free whole-body 0.05 T MRI scanner. (A) Axial abdominal T1W and T2W images from a healthy volunteer (28 years old; male) using 3D SoS GRE (TR/TE/α° = 35 ms/5 ms/70°), and 3D SoS FSE (TR/TE/ETL = 700 ms/111 ms/18), respectively. (B) Axial abdominal DWI image set from a healthy volunteer (27 years old; male) using 2D EPI DWI (TR/TE = 1250 ms/84 ms). Images with $b = 0$ and 300 s/mm 2 are shown, together with computed apparent diffusivity coefficient (ADC) map. (C) Axial abdominal 3D bSSFP images with varying tissue contrasts from the same volunteer as (B) using different flip angles ($\alpha = 50^\circ, 80^\circ$, and 120° with TR = 8 ms). (D) Coronal pelvis T1W and T2W images from a healthy volunteer (28 years old; male) acquired using 3D FSE with TR/TE/ETL = 450 ms/55 ms/7 and 1500 ms/146 ms/23,

Figure 4A displays lung images. Axial bSSFP images were acquired during free breathing using 3D bSSFP sequence (with T2/T1 weighting). Free-breathing axial T2W images were obtained with 3D SoS FSE sequence. Maximum intensity projection (MIP) images are also presented. Pulmonary vessels can be observed in the bSSFP images whereas the parenchyma signal is visible

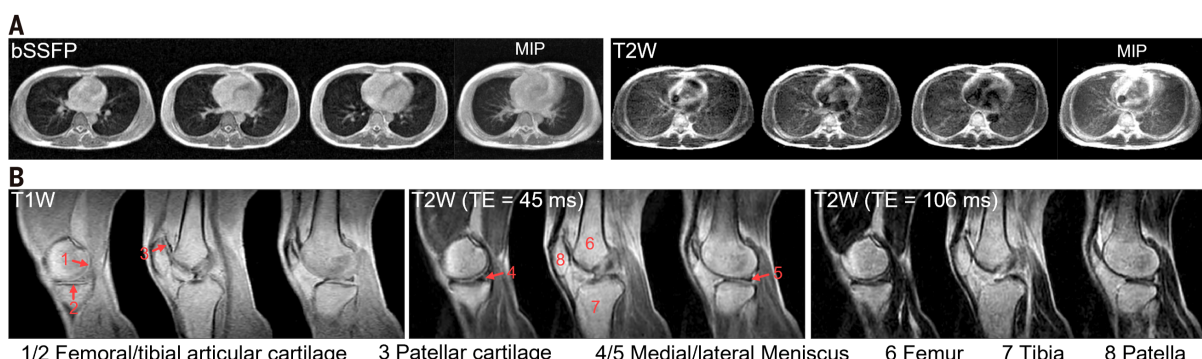
in the T2W images. To demonstrate musculoskeletal imaging, the knee was scanned. Figure 4B shows the sagittal knee TIW and T2W images acquired using cartesian 3D GRE and FSE sequences. Various knee structures such as the patella, femoral and tibial articular cartilage, and lateral and medial meniscus of the posterior horn can be identified in these images.



Downloaded from https://www.science.org at University Van Amsterdam on April 13, 2025

Fig. 4. Typical 0.05 T lung and knee images from healthy adults. (A) Axial lung bSSFP and T2W images from a healthy volunteer (25 years old; male) using 3D bSSFP (TR/α° = 8ms/50°; resolution 2.5×2.5×8.0 mm 3) and 3D SoS

respectively. For each imaging protocol, scan time was 8 min or less. Image resolution was ~2.3×2.3×8.0 mm 3 (~2.3 mm in-plane resolution and 8.0 mm slice thickness) for T1W, T2W, and bSSFP images, ~5.0×5.0×8.0 mm 3 for DWI images by acquisition. All images are displayed at reconstruction resolution 1×1×4 mm 3 .



FSE (TR/TE/ETL = 1000ms/90ms/13; resolution 2.4×2.4×8.0 mm 3), respectively. The corresponding MIP images from 5 consecutive slices are also shown. (B) Sagittal knee T1W and T2W images from a healthy volunteer (34 years old; male) using 3D GRE (TR/TE = 60 ms/6 ms/70°; resolution 1.4×1.9×7.0 mm 3) and 3D FSE (TR/TE/ETL = 420 ms/45 ms/7 and 1500 ms/106 ms/17; resolution 1.9×2.0×7.0 mm 3). Scan time was 8 min or less for each protocol.

Figure 5 presents the free-breathing cardiac cine images and time-of-flight (TOF) magnetic resonance angiography (MRA) from healthy volunteers. Short-axis bright-blood cine was acquired using a electrocardiogram (ECG)-triggered 3D segmented bSSFP sequence from a healthy young volunteer (Fig. 5A). Left ventricle and myocardium can be delineated, and papillary muscle is also visible. As shown in movie S1 the left and right ventricular volumes changed periodically during the cardiac cycle. The estimated volumes were derived from the middle 3 consecutive slices (movie S2). The left ventricle (LV) ejection fraction was estimated to be ~60% from the LV blood cross-sectional areas, which was largely consistent with literature value (31). Figure 5B and movies S3 to S5 present the neck TOF MRA acquired using a 2D flow-compensated GRE sequence. A total of 34 slices with 4 mm thickness were obtained, covering 136 mm in the head/foot direction. With venous blood saturation, major carotid arteries can be clearly observed, including the left and right common carotid arteries, external and internal carotid arteries, as well

as their bifurcations. With arterial blood saturation, major veins such as jugular veins can be readily seen.

Utilizing deep learning for enhanced image formation at 0.05 Tesla

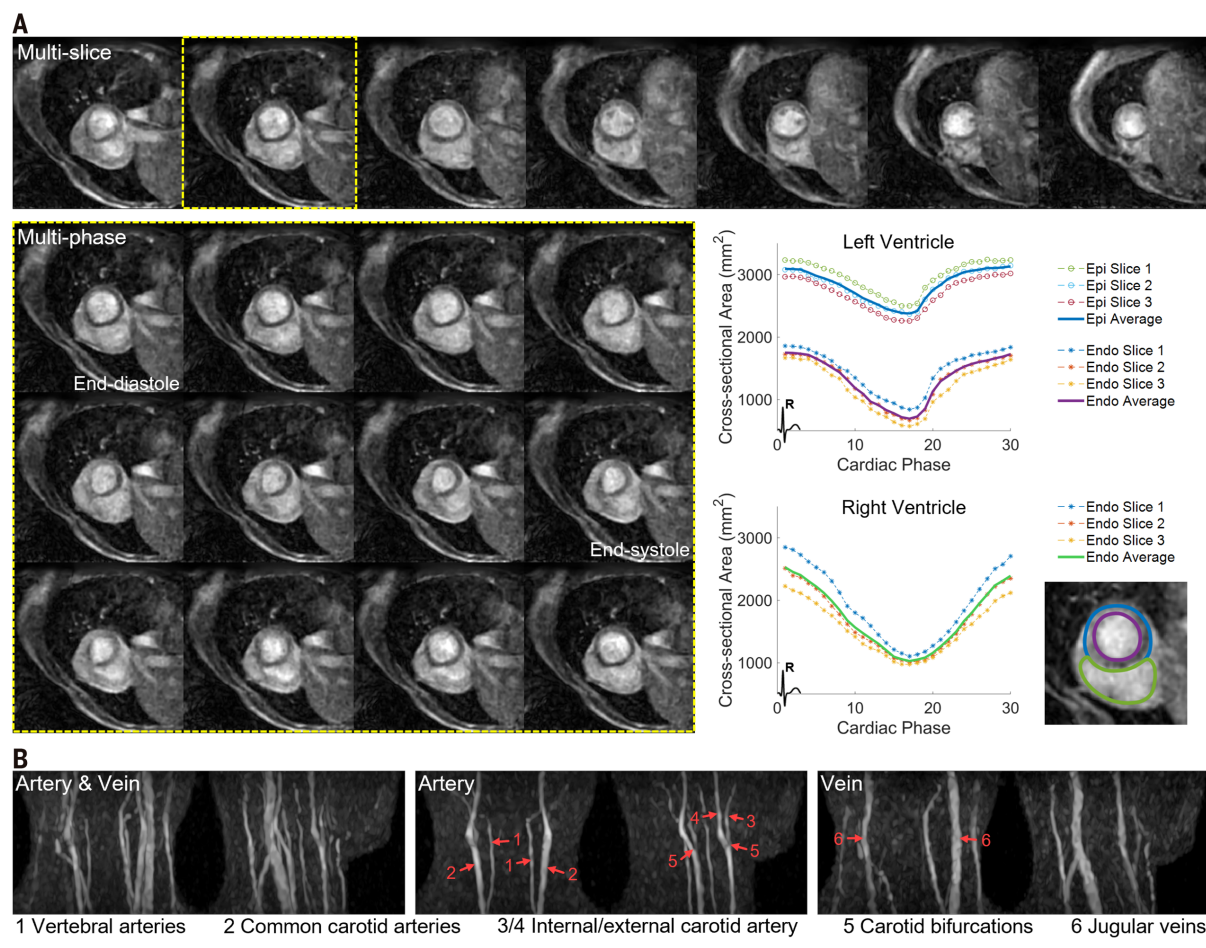
MR signal at 0.05 T is several orders of magnitude weaker than at 3 T, the standard high-field strength, due to its proportionality to field strength squared (B_0^2) (32), causing high image noise and poor resolution in ULF MRI. To overcome this challenge, we turned to computing and devised deep learning-based reconstruction methods for ULF MRI image formation that are driven by the large-scale high-field MRI data (23, 26). We designed a partial Fourier super-resolution (PF-SR) method that integrates image reconstruction and super-resolution (fig. S3) (26). The PF-SR model, consisting of multiscale feature extraction, spatial attention, and reconstruction functions, was experimentally validated by comparing 0.055 T brain images to 3 T images from the same subjects (26). In this study, we demonstrated PF-SR reconstruction for whole-

body MRI at 0.05 T. The data acquisitions typically involved 3D encoding with k-space partial Fourier sampling. See tables S3 to S5 for the data acquisition, model training, and image reconstruction details. By learning the relatively homogeneous human anatomical structures and contrasts readily available in the high-field MRI datasets, the PF-SR reconstruction approach advanced the whole-body 0.05 T image quality by effectively suppressing artifacts and noise and increasing spatial resolution.

Figure 6A and movies S6 and S7 show the brain T1W and T2W images reconstructed using the conventional Fourier method (low resolution LR) and deep learning PF-SR method, alongside high resolution 3 T images obtained from a healthy volunteer. 0.05 T T1W and T2W data were acquired with isotropic 3-mm resolution using 3D FSE sequence with and without inversion recovery preparation and scan time 5.0 and 6.2 mins, respectively. The PF-SR method produced isotropic 1-mm resolution and led to substantially improved 0.05 T image quality in terms of clarity. As confirmed

Fig. 5. Typical 0.05 T heart cine images and neck magnetic resonance angiography (MRA) images from healthy adults.

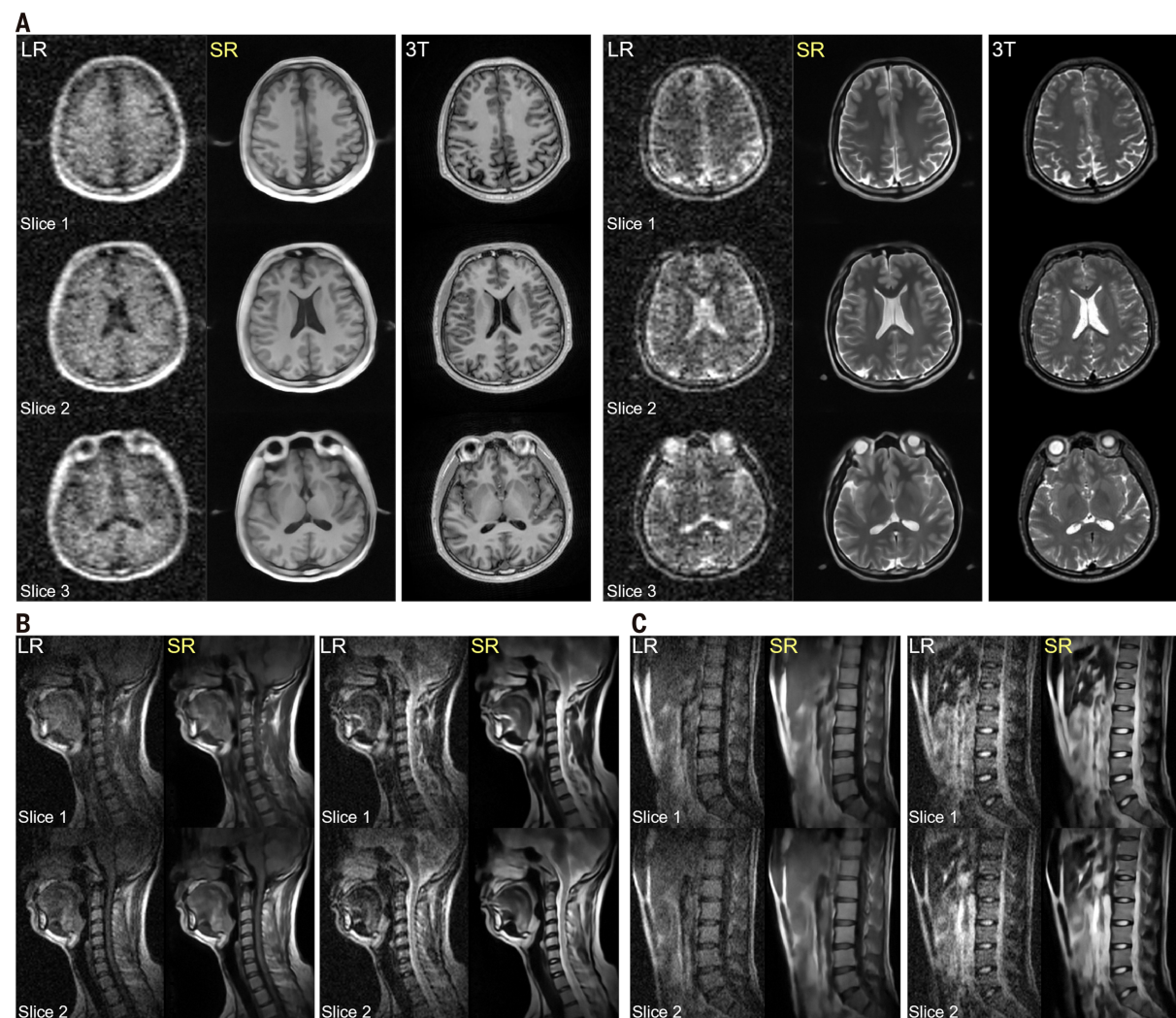
(A) Short-axis bright-blood images from a healthy volunteer (21 years old; male) using ECG-triggered 3D bSSFP ($TR/\alpha^\circ = 8\text{ ms}/70^\circ$; resolution $2.5 \times 2.5 \times 8.0\text{ mm}^3$). Central 7 consecutive slices (with 8-mm thickness) are shown (see movie S1 for cine). The most central slice at 12 cardiac phases (out of the total 30) is displayed. Left ventricle (LV) and right ventricle (RV) volumes during the cardiac



cycle were segmented (see movie S2 for segmentation) and their changes were plotted. They were estimated from the blood cross-sectional areas within the middle 3 consecutive slices. (B) Neck TOF MRA MIP images acquired from a healthy volunteer (34 years old; male) with 2D TOF flow-compensated GRE ($TR/TE/\alpha^\circ = 40\text{ ms}/10\text{ ms}/90^\circ$; resolution $2.0 \times 2.0 \times 4.0\text{ mm}^3$) with no saturation, venous saturation, or arterial saturation, respectively. For each protocol, scan time was 8 min or less.

Fig. 6. Demonstration of deep learning partial Fourier super-resolution (PF-SR) reconstruction for 0.05 T brain and spine imaging.

(A) Axial brain T1W and T2W images were reconstructed using both the conventional 3D Fourier method and the 3D deep learning partial Fourier super-resolution (PF-SR) method from a healthy volunteer (34 years old; male). PF-SR reconstruction extended the original low resolution (LR) $3 \times 3 \times 3$ mm 3 to synthetic super-resolution (SR) $1 \times 1 \times 1$ mm 3 . 3 T MRI images from the same volunteer are also shown for comparison. Note that, to facilitate visual comparison, the 3T dataset was co-registered to 0.05 T dataset



using rigid 3D translations and rotations. (B) Sagittal C-spine T1W and T2W images were reconstructed using the Fourier method (LR) versus the PF-SR method (SR) from the healthy volunteer shown in Fig. 2B, with respective resolution $2.1 \times 2.1 \times 8.0$ mm 3 and $1.0 \times 1.0 \times 4.0$ mm 3 . (C) Sagittal L-spine T1W and T2W images were reconstructed using Fourier method (LR) versus PF-SR method (SR) from

the healthy volunteer shown in Fig. 2C, with respective resolution $2.2 \times 2.3 \times 8.0$ mm 3 and $1.1 \times 1.1 \times 4.0$ mm 3 . See table S3 for details on data acquisition, PF-SR model training, and reconstruction. 0.05 T brain T1W and T2W data were acquired using 3D FSE sequence with and without inversion recovery and scan time 5.0 and 6.4 min, respectively. Scan time for each C- and L-spine protocol was 8 min or less.

by the 3 T results, numerous fine neuroanatomical structures were restored in the PF-SR images. Moreover, various brain anatomical structures appeared complementary in contrast between T1W and T2W images, as expected. Figure 6, B and C, presents the typical T1W and T2W results for the C-spine and L-spine, respectively. Once again, the PF-SR method enhanced the image quality allowing improved visualization of structural details concerning the intervertebral body and disc, spinal cord, and CSF. These brain and spine results were consistent with the testing results using synthetic datasets (figs. S4 and S5 and movies S8 and S9).

Fig. 7A presents the results for abdominal imaging. With PF-SR reconstruction various structural details such as vessels within the liver, kidneys, stomach, pancreas, spleen, and

spine could be easily identified and delineated. Again, these anatomical structures appeared complementary in contrast between T1W and T2W images, as expected. Figure 7B and movie S10 show knee images from a healthy volunteer. PF-SR enabled clearer delineation of key knee structures including the patella, articular cartilage, and meniscus. Overall, these initial PF-SR results indicate the potential and prowess of deep learning PF-SR image reconstruction in advancing ULF MRI of various anatomical structures.

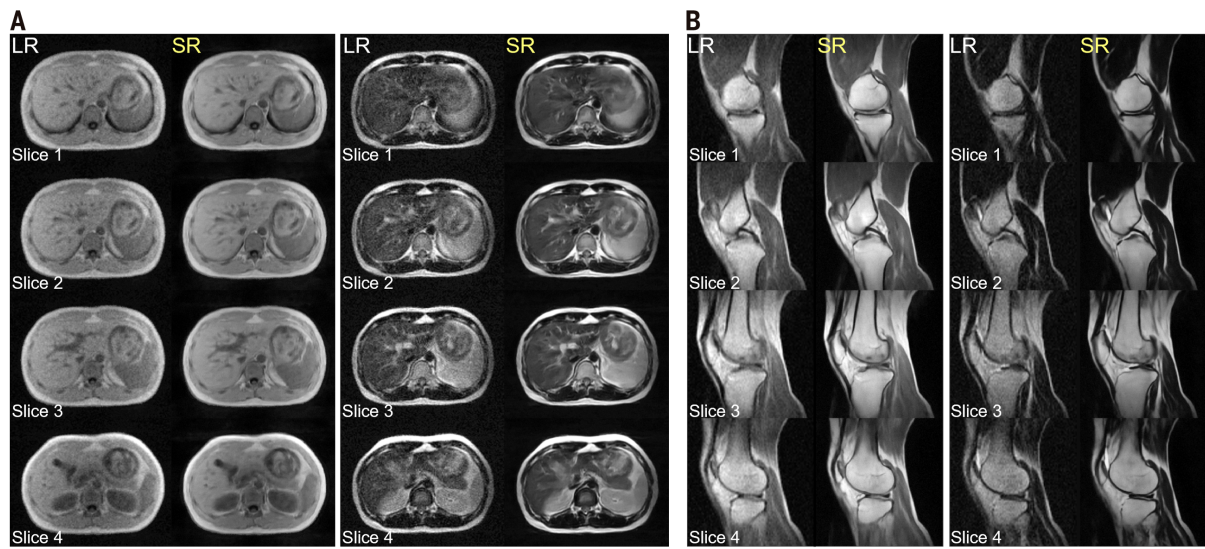
Discussion

We aim to address a critical resource challenge in health care: the limited and scarce access to MRI. Despite over half a century of technology development since the seminal paper published by Paul Lauterbur in 1973 (5), globally,

clinical MRI procedures remain mostly unattainable for over two-thirds of the world's population (6). Historically, the development of MRI technology started at very low fields, with the earliest superconducting or resistive whole-body magnets operating at a field strength of around 0.05 T (33, 34). The first commercial systems, introduced in the early 1980s, reached ~0.5 T. However, the progress in low-field MRI development was halted with the introduction of the first whole-body 1.5 T superconducting scanner by General Electric in 1983 (14). In this study, we revisited 0.05 T whole-body MRI by reducing traditional MRI hardware requirements and harnessing computing power as well as extensive physics and engineering expertise gained over several decades. We developed a low-cost, patient-centric whole-body MRI scanner

Fig. 7. Demonstration of deep learning PF-SR reconstruction for 0.05 T abdominal and knee imaging.

(A) Axial abdominal T1W and T2W images reconstructed using both conventional 3D Fourier method (LR) versus 3D PF-SR method (SR) from the healthy volunteer shown in Fig. 3A. PF-SR method extended the original low resolution



$2.2 \times 2.2 \times 8.0 \text{ mm}^3$ to synthetic super-resolution $1.1 \times 1.1 \times 4 \text{ mm}^3$. (B) Sagittal knee T2W images reconstructed using Fourier method (LR) versus PF-SR method (SR) from the healthy volunteer in Fig. 4B with resolution $1.9 \times 2.0 \times 7.0 \text{ mm}^3$ and $1.0 \times 1.0 \times 3.5 \text{ mm}^3$, respectively. See table S3 for data acquisition, PF-SR model training, and reconstruction details. Scan time for each protocol was 8 min or less.

based on a permanent 0.05 T magnet that operates on a standard AC wall power outlet, without the need for RF or magnetic shielding. This scanner is compact and potentially mobile, and can be manufactured, maintained, and operated at a low cost. We experimentally demonstrated the general utility of such a shielding-free ULF scanner for imaging various human anatomical structures at the whole body level, with acceptable scan time (≤ 8 min per protocol) even in the presence of strong EMI. Moreover, we demonstrated the effectiveness of 3D deep learning image formation in advancing whole-body ULF image quality by leveraging extensive high-field whole-body MRI datasets.

The whole-body ULF MRI scanner demonstrated in this study has the potential to complement existing high-performance high-field clinical MRI, especially in a point-of-care manner. By providing a more affordable and accessible option, whole-body ULF MRI can help expand the availability of MRI scans. ULF MRI offers several distinct advantages that make it an attractive option for patient comfort and safety (12, 35–37). These include an open scanning environment for reduced claustrophobic effect (38, 39), less acoustic noise during scanning for minimizing its potentially adverse effect (12, 40, 41), low sensitivity to metallic implants, less image susceptibility artifacts at air/tissue interfaces, and an extremely low RF specific absorption rate (SAR) (12, 35–37). Moreover, imaging at ULF is attractive because tissues typically exhibit considerably shorter T1 and longer T2 and T2* at ULF (12, 29, 30). This enables more time-efficient data acquisition protocols as a result of faster longitudinal magnetization recovery and slower transverse

magnetization decay, allowing for easy adaptation of SNR-efficient 3D acquisitions, as shown in most protocols in this study.

Additional studies will be essential not only for advancing ULF MRI technology but also for evaluating its clinical efficacy. Recent studies by our group and others, utilizing dedicated 0.055 T and 0.064 T brain ULF MRI scanners, have demonstrated their point-of-care potential in assessing conditions such as ischemic stroke, hemorrhage, brain tumors, brain injuries, and multiple sclerosis (12, 15, 16, 19, 42). The present study further highlights the feasibility of imaging the C- and L-spine, another crucial central nervous system (CNS) component. Because MRI is regarded as the preferred imaging modality for the CNS due to its exceptional soft tissue contrasts (5), we foresee the potential application of whole-body ULF MRI in neurology clinics, trauma centers, neurosurgical suites, and neonatal/pediatric centers.

Whole-body MRI is valuable in diagnosing and characterizing various types of cancers, such as liver, prostate, pancreatic, breast, and colorectal cancer (43–48). Liver cancer, for instance, is one of the most common malignancies worldwide, with 900,000 new cases and 830,000 deaths reported in 2020 alone. Hepatocellular carcinoma (HCC) is the most prevalent primary liver cancer, often diagnosed at advanced stages, resulting in poor prognosis (49). Recent studies have demonstrated the effectiveness of simplified MRI protocols (T1W, T2W, and DWI) for HCC screening (50, 51). Moreover, MRI techniques such as magnetic resonance elastography and liver fat quantification have shown their efficacy in evaluating liver stiffness and steatosis, respectively, for HCC prognostication (45, 52, 53). In fact, these

two MRI techniques can be potentially realized on our whole-body ULF MRI scanner to characterize diffuse liver diseases, despite the low SNR at ULF (54, 55). In addition to the CNS and abdomen, whole-body ULF MRI is valuable in assessing joints such as knees and shoulders. Additionally, cardiac late gadolinium enhancement, T1- and T2-mapping protocols are particularly effective in assessing myocardial viability and myocarditis (56, 57). We anticipate that future technical development and clinical evaluation of these ULF MRI protocols will address numerous clinical needs in a point-of-care manner.

Over the past half century, MRI has evolved from a basic concept (1) to an indispensable nonionizing medical imaging modality with wide-ranging applications in diagnosing and prognosis abnormalities in the CNS, abdomen, musculoskeletal, and cardiovascular systems (14, 27). Owing to its soft tissue contrasts and multiparametric nature, MRI is often preferred over other imaging modalities. Despite being regarded as one of the most notable technological advancements in modern health care (3), the overall usage of MRI ranks below computed tomography (CT), partly due to the greater accessibility of CT scans. Nevertheless, we argue that MRI offers the ultimate advantage of not using ionizing radiation, making it a safer option for patients. In particular, MRI is a preferred modality for repeated imaging or for vulnerable populations such as children and pregnant women. ULF MRI may also potentially play a role in image-guided biopsy or structure-sensitive treatment procedures (58–62), where continuous or repeated imaging is necessary.

However, advancing image quality and scan speed remains a major technical challenge for

ULF MRI. The ability of ULF MRI to differentiate various soft tissues and characterize pathologies under clinical conditions is determined by image quality and scan speed. It is crucial for ULF MRI to have adequate spatial resolution and contrast while maintaining a reasonable scan time, even in the presence of physiological motions. This is particularly important considering the availability of other imaging modalities such as ultrasound and x-ray, which are cheaper and faster. Therefore, future ULF MRI developments should encompass data acquisition and image formation, hardware components, and eventually clinical optimization and utilization.

Deep learning presently powers numerous advances in computational science and engineering (20, 21), including imaging (63). Deep learning will likely fuel future ULF MRI development through data-driven image reconstruction to tackle the SNR challenge. Traditional MRI data acquisition and image reconstruction methods do not rely on any prior knowledge on human anatomy, despite the relatively homogeneous and genetically predefined anatomical structures and tissue contrasts exhibited through various imaging protocols. By using such prior information through deep learning, it is plausible to boost ULF MRI quality and speed, allowing for more intelligent image formation beyond traditional Fourier or compressed sensing reconstruction. Recent studies from our group (23, 26) and others (22) have demonstrated the possibility of a deep learning MRI reconstruction and super-resolution approach for brain ULF MRI by exploiting large-scale high-field brain MRI data. In this study, we have implemented and demonstrated such an image formation method, PF-SR (26), applied to brain, spine, liver, and knee imaging, illustrating the ability of such data-driven image formation in enhancing image resolution while suppressing noise and artifacts. Our previous studies (23, 26) and the preliminary brain and spine tests using synthetic datasets in this study have also shown the potential of applying this approach to datasets that contain brain and spine lesions.

However, the fidelity of the PF-SR method in restoring 3D image details remains to be carefully evaluated and optimized for each anatomical structure and contrast. As an end-to-end supervised super-resolution approach, the PF-SR image formation is prone to both blurring and structural hallucinations to a certain extent, especially in regions with fine details but low SNR and contrast (23, 26, 64). In fact, hallucinations can be seen among some sulci and gyri near the brain edge in the TIW PF-SR results shown in Fig. 6A. These hallucinations likely arose from the low SNR and poor contrast in the raw 3D ULF data. Hallucination level can increase with decreasing SNR and contrast in the input data. The effective-

ness of the PF-SR method in restoring image details is limited by the interplay between noise (and unseen artifacts not accounted for during training) and predicting 3D image details using prior knowledge of specific anatomical MRI data. This prior knowledge is deeply ingrained within the PF-SR models, which are trained to learn the structural and contrast 3D multiscale features from a large collection of standard human MR images specific to a particular organ and MRI contrast. Future research should also optimize and evaluate the capabilities of PF-SR in detecting various pathologies. To augment the PF-SR model training, we can include a diverse range of synthetic datasets that include lesions of different types, extents, and locations. This will help ensure its robustness in clinical diagnostic applications. Additionally, it may be necessary to acquire and compare both experimental ULF and high-field MRI data from the same patients to directly validate the sensitivity and specificity of the PF-SR method in detecting specific lesions. Ultimately, it is imperative to find a balance between clinical value, PF-SR output resolution and fidelity, and quality of input image data.

The extremely low SNR of MR signal at ULF continues to be a major challenge. MR signal is proportional to B_0^2 whereas the SNR scales approximately with $B_0^{7/4}$ at low field (32, 37, 65). Consequently, SNR at 0.05 T is about three orders of magnitude lower compared with 3 T. Future ULF MRI hardware development may focus on more sensitive MRI receive coils and/or more intelligent signal reception approaches at RF megahertz range through design and/or material innovation, which is a topic largely unexplored in past development of high-field MRI. For human imaging at ULF, noise in MR signals is primarily dominated by the RF receive coil noise. Therefore, SNR can be substantially increased by cooling the RF receive coil and preamplifier, potentially through cryogenic cooling or cryogen-free conduction cooling using cryocoolers (66, 67). Notably, such an approach substantially increases the coil Q factor, thus reducing the effective coil signal detection bandwidth and potentially limiting high acquisition bandwidth sequences like EPI DWI at ULF.

As a low-cost, point-of-care, and patient-friendly device, whole-body ULF MRI should operate without any enclosed RF shielding. In this study, we have successfully developed and deployed the Deep-DSP approach (25), which directly predicts EMI-free MR signals even in the presence of very strong EMI signals from external environments and internal electronics. The Deep-DSP strategy (25) functions with or without dedicated EMI characterization data, considerably outperforming all existing analytical or deep learning methods that have been recently developed by our group (12, 18) and others (17). The Deep-DSP

method, as illustrated in fig. S1, eliminates the need for the EMI subtracting procedure utilized in CNN (12, 18) and EDITER (17) methods. This removal of the subtraction procedure mitigates the potential error propagation associated with it. The residual U-Net architecture of the Deep-DSP method is deeper and more adaptable compared with a simple CNN (12, 18), enabling better learning of the complex relationships between EMI signals among coils. Moreover, the Deep-DSP model, trained on synthetic data, can capture the characteristic differences between EMI signals and MR k-space signals, unlike the CNN and EDITER methods. Collectively, these factors contribute to the enhanced performance of EMI elimination achieved by the Deep-DSP method. Nonetheless, it remains imperative to continuously develop more effective methods to address complex EMI signals. Several factors contribute to this need: First, EMI signals can originate from multiple and diverse sources. Second, both MRI receive and sensing coils are unavoidably subject to baseline electronic noise, which interferes with reliably probing the electromagnetic coupling between the MRI receive coil and EMI sensing coils. Third, the EMI signal propagation chain may exhibit nonlinear responses. Last, EMI source locations and/or surrounding environments may change dynamically during scanning. These largely intractable issues require further development of robust EMI elimination strategies using data-driven approaches, especially for extremely strong and diverse EMI sources that may be encountered in unshielded whole-body imaging scenarios or in proximity to other electrical devices.

An ideal whole-body ULF MRI scanner should be lightweight and have a small fringe magnetic field. Our current prototype scanner was designed primarily for conceptual demonstration without extensive hardware optimization, resulting in a relatively heavy magnet (~1300 kg) though the scanner could still be potentially mobile if equipped with a battery-operated motor system, similar to a clinical mobile CT scanner. A recent 0.2 T magnet design for brain MRI has demonstrated the possibility of reducing the double-plate magnet weight by omitting the horizontal iron poles while adding side vertical magnetic poles (68). With this concept and implementation of non-iron yokes, we estimate that our whole-body 0.05 T magnet weight could be substantially reduced to ~600 kg, rendering the entire scanner mobile. Future whole-body magnet development may also explore the use of low-weight homogenous cylindrical Halbach magnet designs (9, 11), while prioritizing a relatively large inner magnet diameter and small fringe field to ensure openness and patient comfort. Implementing such an approach could greatly reduce the magnet weight and size but it may be necessary to

address the magnet thermal and structural stability issues.

In conclusion, we addressed the challenge of limited MRI accessibility by developing an affordable, simple, and computing-powered whole-body 0.05 T MRI scanner. Our low-power, compact scanner was designed to operate from a standard AC wall power outlet, without the need for RF or magnetic shielding. We demonstrated the versatility of the ULF MRI for imaging various human anatomical structures. Moreover, we demonstrated the potential of 3D deep learning reconstruction to substantially augment ULF image quality by exploiting computing power and extensive high-field MRI data. These advancements will pave the way for affordable, patient-centric, and site-agnostic MRI scanners, addressing unmet clinical needs in various health care settings globally.

Materials and Methods

Shielding-free whole-body MRI hardware design

The magnet design features two plates connected by four vertical pillars to optimize openness and patient comfort (Fig. 1A). Essential components such as the NdFeB magnet (N50), iron yoke (Q235A), pole (pure iron DT4C), silicon steel anti-eddy current plate (30ZH105), and passive shimming ring (pure iron DT4C) were developed using electromagnetic field modeling to create a uniform 0.05 T field suitable for whole-body imaging while maintaining shoulder and chest accessibility. The magnet assembly weighed ~1300 kg. Although a cylindrical Halbach magnet could offer a lighter weight and smaller fringe field (9, 11), we chose this open double-plate design for its structural openness and patient comfort. To achieve a homogeneous field, pole pieces and shimming rings were used, along with additional passive shimming by incorporating small iron and/or NdFeB pieces, through iterative 3D field mapping and compensation. The final exterior dimensions of the magnet were 114.0 cm × 102.6 cm × 69.8 cm (width × length × height), featuring a 40 cm clear vertical gap and 92 cm width for patient entry. The final magnetic field was 0.048 T at a room temperature of 25°C, corresponding to a 2.045 MHz proton resonance frequency. The field exhibited an inhomogeneity of less than 200 ppm peak-to-peak across an oblate ellipsoid volume with a diameter of 40 cm and a height of 38 cm. The anti-eddy current plate effectively reduced overall eddy currents to below 1% in all three directions before applying any pre-emphasis compensation. The reduction made it possible to implement more advanced and hardware-demanding imaging sequences, such as EPI and bSSFP. The 5 Gauss fringe field was contained within 104 cm, 114 cm, and 104 cm from the magnet center in the width, length, and height directions, respectively (Fig. 1B). The total physical footprint

of the scanner, including both the magnet assembly and electronic cabinet but excluding the detachable patient bed, was ~1.3 m². Note that the basic structural design of this 0.05 T magnet was conceptually similar to our earlier 0.055 T magnet for brain MRI except for the iron support structure (12).

Note that the most commonly used rare earth magnet material NdFeB was chosen here over the samarium cobalt (used in recent brain ULF MRI magnet designs by our group (12) and commercial company Hyperfine) because it offers a higher BH_{max} of 35 to 50 MGoe compared with 22 MGoe for SmCo and it costs less. Despite its relatively poor temperature stability of -0.125%/°C compared with 0.015%/°C for SmCo (69, 70), the main magnetic field and homogeneity remained adequately stable in a standard 25°C laboratory environment (without special air conditioning) and during scanning.

Planar gradient coils, made from rectangular wire, were secured to epoxy resin boards to preserve their winding patterns. Whereas Gx and Gy gradient coils were unshielded, Gz coil was actively shielded. Gx, Gy, and Gz coils had resistances of 83.2 mΩ, 84.5 mΩ, and 130.8 mΩ, and inductances of 280.3 μH, 254.8 μH, and 232.2 μH, respectively. Their sensitivities were 12.5 mT/m/100A, 13.0 mT/m/100A, and 6.3 mT/m/100A, respectively. A PCI GAI50 switching amplifier (Performance Control Inc.), with a peak current of 150 A and a peak voltage of 150V, was used to drive the gradient coils.

Planar RF coil served as a separate transmit coil with Q factor of ~13 and ~14 when loaded and unloaded, respectively. A number of RF receive coils were constructed using the standard solenoid design (65, 71), including three single-channel solenoid coils for brain imaging (12) (200 mm by 229 mm; 8 winding turns with loaded Q of ~38), C-spine imaging (204 mm by 220 mm; 8 winding turns with loaded Q of ~49), chest and abdominal imaging (280 mm by 350 mm; 10 winding turns with loaded Q of ~37). A decoupling circuit was also implemented to detune the receive coil during RF transmission. MR signal was passed through a two-stage preamplifier module (~20 dB each). Note that, at 0.05 T, RF transmit coil was typically driven by very low RF power. For example, the nonselective 1-ms 90° block pulse only required ~100 W peak RF power, incurring negligible SAR as expected (12, 35–37). Gradient/RF subsystems and data acquisition were controlled by a PC-based multichannel NMR spectrometer console (EVO Spectrometer; www.mrsolutions.com).

Deep learning EMI Elimination by deep-DSP

We utilized a deep learning method, Deep-DSP, developed by our group for mobile brain MRI scanners (25). Ten small EMI sensing coils (LC-resonant loops with 5 cm diameter) were placed near the patient bed and magnet

and inside the electronic cabinet close to the gradient amplifier and console.

Deep-DSP was designed to predict EMI-free MR signals directly from the signals simultaneously detected by the MRI receive coil and EMI sensing coils (Fig. 1C and fig. S1). During scanning, the MRI receive coil and EMI sensing coils simultaneously sampled data within two windows: one for MR signal acquisition and the other for EMI signal characterization acquisition. A residual U-Net model was then trained using synthetic MRI receive coil data and EMI sensing coil data obtained during the EMI signal characterization window (25). Note that the synthetic MRI receive coil data here were formed by adding the experimental EMI signals (from MRI receive coil during EMI characterization window) to a set of EMI-free brain 3 T k-space data that were arbitrarily chosen (25) (fig. S1). Once trained, the model was used to directly predict EMI-free MR signals from the signals simultaneously collected by the MRI receive and sensing coils during the MR signal acquisition window. The U-Net model, trained using the Adam optimizer (72), minimized L1 loss with parameters such as batch size 64, learning rate 0.0002, β1 0.9, and β2 0.999 for 40 epochs. The average training time was ~3 min per imaging protocol on an Nvidia A100 GPU with PyTorch 2.0.1 and CUDA 11.8 on Ubuntu 22.04, which could be further shortened through both training and code optimization.

Note that, in Deep-DSP, the EMI signal characterization window was not strictly necessary. In this study, the EMI signal characterization window was specifically implemented for the 3D FSE and 2D EPI DWI sequences. To maintain the minimal TR, the EMI signal characterization window was not implemented for all other sequences. Instead, the outer 50% k-space data collected during the MR signal acquisition window served as an alternative EMI characterization data for training the model, exhibiting no noticeable performance degradation.

ULF MRI scan protocols and optimization

Several most commonly used imaging sequences were implemented and optimized, including cartesian 3D FSE/GRE/bSSFP, cartesian 2D EPI-based DWI, and 3D SoS FSE and GRE with golden-angle radial sampling. All protocols were free-breathing. For cardiac imaging, cartesian 3D bSSFP sequence was ECG-triggered using a peripheral finger pulse oximeter. We implemented T1-weighted, T2-weighted, FLAIR-like (12), and DW contrasts that are most common for clinical high-field MRI. For brain and abdominal DWI, both EPI Nyquist ghosts and field inhomogeneity related geometric distortions were corrected when reconstructing b_0 ($b = 0$) and b_1 images (with $b \neq 0$ in s/mm²) (12). Non-contrast Neck TOF MRA used a 2D GRE sequence with 1st-order flow

compensation in both slice selection and frequency encoding directions, with or without venous or arterial saturation. All images were reconstructed to higher display resolution by zero padding in k-space. Reconstruction was performed with standard Fourier transform together with iterative projection onto convex set (POCS) (26, 73) for partial Fourier sampling whenever applicable, except for 3D SoS radial sampling where filtered backprojection reconstruction was used. Image denoising was typically performed after image reconstruction using the standard block matching with 4D filtering (BM4D) (74). For cardiac cine analysis, left and right ventricles were segmented in a semi-automatic manner using Segment CMR software (<https://medviso.com/cmr/>). The left ventricle ejection fraction was computed by (ESV/EDV)x100%, where ESV and EDV refer to the left ventricular volume at end-systole and end-diastole, respectively, which were estimated from the middle three consecutive short-axis slices. The data acquisition and image reconstruction details for various anatomical regions (brain, C-spine, L-spine, abdomen, pelvis, lung, knee, heart, and neck MRA) can be found in table S2.

Deep learning 3D PF-SR image reconstruction

PF-SR, a deep learning reconstruction method developed by us (26), was applied to imaging of the brain, spine, abdomen, and knee on the 0.05 T whole-body MRI scanner. PF-SR method first acquired a 3D k-space dataset using incomplete or partial Fourier sampling in k-space, then a low-resolution 3D image dataset (as input dataset) was formed by simple 3D Fourier transform. Following this, a high-resolution 3D image dataset was reconstructed using a fully 3D, end-to-end, image-domain deep learning model. This PF-SR model was specifically optimized, trained and validated for specific anatomical structure and image contrast, utilizing synthetic 3D ULF data that were simulated from the corresponding large-scale high-resolution high-field (1.5 T or 3 T) MRI data.

The overall PF-SR model architecture is illustrated in fig. S3. In brief, the model applied multi-scale feature extraction with a residual group (RG) inspired by the residual channel attention network (75) and a modified residual channel attention block for extracting multi-scale high-level features (23). Small kernel sizes at the top scale level enabled local image feature extraction, whereas an increased receptive field of 3D convolution layers at middle to bottom scale levels facilitated semi-global image feature learning (76–78). Channel and spatial attentions were utilized to modulate high-level features based on their inter-channel and inter-spatial relationships (79). The modulated features were then fed into a cascade of RGs, up-sampled to a high-resolution feature space using a 3D sub-pixel convolution layer, and

transformed into a high-resolution 3D image residue using a 3D convolution layer (23). The final high-resolution 3D image output was generated by combining the image residue and trilinearly up-sampled model input. The PF-sampled low-resolution noisy 3D T1W and T2W ULF data were synthesized as described in the recent PF-SR study (26) from the corresponding high-resolution high-field data (80–82) (see details in tables S3 and S4). They were used for model training, validation, and testing. Each model typically contained approximately 30 million learnable parameters, and took 2 to 8 hours to train using four Nvidia A100 GPUs.

This 3D super-resolution strategy, initially demonstrated for a factor of x2 with isotropic resolution in both model input and output (23, 26), is also applicable to anisotropic resolution and super-resolution factors at x2 or x3. In this study, T1W and T2W models were trained for brain, C-spine, L-spine, abdomen, and knee imaging and applied to corresponding datasets acquired experimentally on the 0.05 T whole-body scanner. The PF-SR models were obtained using the same model architecture and training procedure. The learning rate was adjusted based on the size of the training data. To evaluate the models, we tested them using synthetic ULF data generated from high-resolution high-field MRI data. Additionally, we compared our PF-SR method to a traditional non-deep learning method (non-DL), which involved using 2D POCS (83) for PF reconstruction, followed by BM4D denoising (74) and tricubic interpolation. We conducted a quantitative evaluation by calculating the 3D structural similarity index measure (SSIM) (84) and the normalized root mean square error (NRMSE). Tables S3 and S4 summarize the raw data acquisition parameters, sources, and sizes of large-scale high-field MRI data used for model training, training times, and super-resolution parameters. Note that only 0.05 T brain T1W and T2W data were acquired with $3\text{ mm} \times 3\text{ mm} \times 3\text{ mm}$ isotropic acquisition resolution to produce 1 mm^3 isotropic synthetic image resolution with x3 super-resolution factor. All other data acquisitions remained the same as described in table S2. The acquisition parameters for high-field MRI datasets (for synthesizing PF-SR training data) are summarized in table S4.

Study participants

A total of 30 healthy volunteers (23 to 77 years old) were recruited for 0.05 T MRI scanning of various anatomical structures with different contrasts. Some of these volunteers were also involved during the initial protocol optimization tasks. Written informed consent was obtained from all participants before each scan, with approval from Institutional Review Board of the University of Hong Kong/Hospital Au-

thority Hong Kong West Cluster. To directly evaluate brain T1W and T2W PF-SR results from 0.05 T, some volunteers were also scanned using a clinical GE 3 T MRI scanner (Signa Premier) with protocol details listed in table S5. A simple rigid 3D co-registration (FSL version 6.0.4) with 3D translations and rotations was performed on the 3 T brain image data to match the orientations of the 0.05 T brain image data, allowing for convenient visual comparison in Fig. 6A. Note the image distortions due to imaging gradient nonlinearities were not calibrated and corrected on our 0.05 T whole-body scanner.

REFERENCES AND NOTES

- P. C. Lauterbur, Image Formation by Induced Local Interactions - Examples Employing Nuclear Magnetic-Resonance. *Nature* **242**, 190–191 (1973). doi: [10.1038/242190a0](https://doi.org/10.1038/242190a0)
- P. Mansfield, A. A. Maudsley, Medical Imaging by Nmr, Medical imaging by NMR. *Br. J. Radiol.* **50**, 188–194 (1977). doi: [10.1259/0007-1285-50-591-188](https://doi.org/10.1259/0007-1285-50-591-188); pmid: [84950](https://pubmed.ncbi.nlm.nih.gov/4950)
- V. R. Fuchs, H. C. Sox Jr., Physicians' views of the relative importance of medical innovations. *Health Aff.* **20**, 30–42 (2001). doi: [10.1377/hlthaff.20.5.30](https://doi.org/10.1377/hlthaff.20.5.30); pmid: [11558715](https://pubmed.ncbi.nlm.nih.gov/11558715)
- Magnetic resonance imaging (MRI) exams (OECD, 2024); doi: [10.1787/1d89353f-en](https://doi.org/10.1787/1d89353f-en)
- R. R. Edelman, S. Warach, Magnetic resonance imaging (1). *N. Engl. J. Med.* **328**, 708–716 (1993). doi: [10.1056/NEJM199303113281008](https://doi.org/10.1056/NEJM199303113281008); pmid: [8433731](https://pubmed.ncbi.nlm.nih.gov/8433731)
- Magnetic resonance imaging (MRI) units (OECD, 2024); doi: [10.1787/1a72e7d1-en](https://doi.org/10.1787/1a72e7d1-en)
- A. Webb, J. Obungoloch, Five steps to make MRI scanners more affordable to the world. *Nature* **615**, 391–393 (2023). doi: [10.1038/d41586-023-00759-x](https://doi.org/10.1038/d41586-023-00759-x); pmid: [36918678](https://pubmed.ncbi.nlm.nih.gov/36918678)
- M. Naddaf, One MRI for 4.7 million people: The battle to treat Syria's earthquake survivors. *Nature* **615**, 193–194 (2023). doi: [10.1038/d41586-023-00547-7](https://doi.org/10.1038/d41586-023-00547-7); pmid: [36849818](https://pubmed.ncbi.nlm.nih.gov/36849818)
- C. Z. Cooley et al., A portable scanner for magnetic resonance imaging of the brain. *Nat. Biomed. Eng.* **5**, 229–239 (2021). doi: [10.1038/s41551-020-00641-5](https://doi.org/10.1038/s41551-020-00641-5); pmid: [33230306](https://pubmed.ncbi.nlm.nih.gov/33230306)
- Y. He et al., Use of 2.1 MHz MRI scanner for brain imaging and its preliminary results in stroke. *J. Magn. Reson.* **319**, 106829 (2020). doi: [10.1016/j.jmr.2020.106829](https://doi.org/10.1016/j.jmr.2020.106829); pmid: [32987217](https://pubmed.ncbi.nlm.nih.gov/32987217)
- T. O'Reilly, W. M. Tieuwisse, D. de Gans, K. Koolstra, A. G. Webb, In vivo 3D brain and extremity MRI at 50 mT using a permanent magnet Halbach array. *Magn. Reson. Med.* **85**, 495–505 (2021). doi: [10.1002/mrm.28396](https://doi.org/10.1002/mrm.28396); pmid: [32627235](https://pubmed.ncbi.nlm.nih.gov/32627235)
- Y. Liu et al., A low-cost and shielding-free ultra-low-field brain MRI scanner. *Nat. Commun.* **12**, 7238 (2021). doi: [10.1038/s41467-021-27317-1](https://doi.org/10.1038/s41467-021-27317-1); pmid: [34907181](https://pubmed.ncbi.nlm.nih.gov/34907181)
- W. T. Kimberly et al., Brain imaging with portable low-field MRI. *Nat. Rev. Bioeng.* **1**, 617–630 (2023). pmid: [37057171](https://pubmed.ncbi.nlm.nih.gov/37057171)
- J. Hennig, An evolution of low-field strength MRI. *Magn. Reson. Mater. Phys.* **36**, 335–346 (2023). doi: [10.1007/s10334-023-01104-z](https://doi.org/10.1007/s10334-023-01104-z); pmid: [37289275](https://pubmed.ncbi.nlm.nih.gov/37289275)
- M. H. Mazurek et al., Portable, bedside, low-field magnetic resonance imaging for evaluation of intracerebral hemorrhage. *Nat. Commun.* **12**, 5119 (2021). doi: [10.1038/s41467-021-2541-6](https://doi.org/10.1038/s41467-021-2541-6); pmid: [34433813](https://pubmed.ncbi.nlm.nih.gov/34433813)
- M. M. Yuen et al., Portable, low-field magnetic resonance imaging enables highly accessible and dynamic bedside evaluation of ischemic stroke. *Sci. Adv.* **8**, eabm3952 (2022). doi: [10.1126/sciadv.abm3952](https://doi.org/10.1126/sciadv.abm3952); pmid: [35442729](https://pubmed.ncbi.nlm.nih.gov/35442729)
- S. A. Srinivas et al., External Dynamic Interference Estimation and Removal (EDITOR) for low field MRI. *Magn. Reson. Med.* **87**, 614–628 (2022). doi: [10.1002/mrm.28992](https://doi.org/10.1002/mrm.28992); pmid: [34480778](https://pubmed.ncbi.nlm.nih.gov/34480778)
- Y. Zhao, L. Xiao, Y. Liu, A. T. Leong, E. X. Wu, Electromagnetic interference elimination via active sensing and deep learning prediction for radiofrequency shielding-free MRI. *NMR Biomed.* **e4956** (2023). doi: [10.1002/nbm.4956](https://doi.org/10.1002/nbm.4956); pmid: [37088894](https://pubmed.ncbi.nlm.nih.gov/37088894)
- K. N. Sheth et al., Assessment of Brain Injury Using Portable, Low-Field Magnetic Resonance Imaging at the Bedside of Critically Ill Patients. *JAMA Neurol.* **78**, 41–47 (2020). doi: [10.1001/jamaneurol.2020.3263](https://doi.org/10.1001/jamaneurol.2020.3263); pmid: [32897296](https://pubmed.ncbi.nlm.nih.gov/32897296)

20. Y. LeCun, Y. Bengio, G. Hinton, Deep learning. *Nature* **521**, 436–444 (2015). doi: [10.1038/nature14539](https://doi.org/10.1038/nature14539); pmid: [26017442](https://pubmed.ncbi.nlm.nih.gov/26017442/)
21. E. J. Topol, As artificial intelligence goes multimodal, medical applications multiply. *Science* **381**, adk6139 (2023). doi: [10.1126/science.adk6139](https://doi.org/10.1126/science.adk6139); pmid: [37708283](https://pubmed.ncbi.nlm.nih.gov/37708283/)
22. J. E. Iglesias et al., Quantitative Brain Morphometry of Portable Low-Field-Strength MRI Using Super-Resolution Machine Learning. *Radiology* **306**, e220522 (2023). doi: [10.1148/radiol.220522](https://doi.org/10.1148/radiol.220522); pmid: [36346311](https://pubmed.ncbi.nlm.nih.gov/36346311/)
23. V. Lau et al., Pushing the limits of low-cost ultra-low-field MRI by dual-acquisition deep learning 3D superresolution. *Magn. Reson. Med.* **90**, 400–416 (2023). doi: [10.1002/mrm.29642](https://doi.org/10.1002/mrm.29642); pmid: [37010491](https://pubmed.ncbi.nlm.nih.gov/37010491/)
24. T. Guillart-Naval et al., Portable magnetic resonance imaging of patients indoors, outdoors and at home. *Sci. Rep.* **12**, 13147 (2022). doi: [10.1038/s41598-022-17472-w](https://doi.org/10.1038/s41598-022-17472-w); pmid: [35907975](https://pubmed.ncbi.nlm.nih.gov/35907975/)
25. Y. Zhao, L. Xiao, J. Hu, E. X. Wu, Robust EMJ elimination for RF shielding-free MRI through deep learning direct MR signal prediction. *Magn. Reson. Med.mrm.30046* (2024). doi: [10.1002/mrm.30046](https://doi.org/10.1002/mrm.30046); pmid: [38376455](https://pubmed.ncbi.nlm.nih.gov/38376455/)
26. C. Man et al., Deep learning enabled fast 3D brain MRI at 0.055 tesla. *Sci. Adv.* **9**, ead9327 (2023). doi: [10.1126/sciadv.ad9327](https://doi.org/10.1126/sciadv.ad9327); pmid: [37738341](https://pubmed.ncbi.nlm.nih.gov/37738341/)
27. P. Börnert, D. G. Norris, A half-century of innovation in technology-preparing MRI for the 21st century. *Br. J. Radiol.* **93**, 20200113 (2020). doi: [10.1259/bjr.20200113](https://doi.org/10.1259/bjr.20200113); pmid: [32496816](https://pubmed.ncbi.nlm.nih.gov/32496816/)
28. L. Feng et al., Golden-angle radial sparse parallel MRI: Combination of compressed sensing, parallel imaging, and golden-angle radial sampling for fast and flexible dynamic volumetric MRI. *Magn. Reson. Med.* **72**, 707–717 (2014). doi: [10.1002/mrm.24980](https://doi.org/10.1002/mrm.24980); pmid: [24142845](https://pubmed.ncbi.nlm.nih.gov/24142845/)
29. P. A. Bottomley, T. H. Foster, R. E. Argersinger, L. M. Pfeifer, A review of normal tissue hydrogen NMR relaxation times and relaxation mechanisms from 1-100 MHz: Dependence on tissue type, NMR frequency, temperature, species, excision, and age. *Med. Phys.* **11**, 425–448 (1984). doi: [10.1118/1.1595535](https://doi.org/10.1118/1.1595535); pmid: [6482839](https://pubmed.ncbi.nlm.nih.gov/6482839/)
30. T. O'Reilly, A. G. Webb, In vivo T_1 and T_2 relaxation time maps of brain tissue, skeletal muscle, and lipid measured in healthy volunteers at 50 mT. *Magn. Reson. Med.* **87**, 884–895 (2022). doi: [10.1002/mrm.29009](https://doi.org/10.1002/mrm.29009); pmid: [34520068](https://pubmed.ncbi.nlm.nih.gov/34520068/)
31. N. Kawel-Boehm et al., Reference ranges ("normal values") for cardiovascular magnetic resonance (CMR) in adults and children: 2020 update. *J. Cardiovasc. Magn. Reson.* **22**, 87 (2020). doi: [10.1186/s12968-020-00683-3](https://doi.org/10.1186/s12968-020-00683-3); pmid: [33308262](https://pubmed.ncbi.nlm.nih.gov/33308262/)
32. D. I. Hoult, R. Richards, The signal-to-noise ratio of the nuclear magnetic resonance experiment. *Journal of Magnetic Resonance (1969)* **24**, 71–85 (1976). doi: [10.1016/j.jmr.2011.09.018](https://doi.org/10.1016/j.jmr.2011.09.018); pmid: [22152352](https://pubmed.ncbi.nlm.nih.gov/22152352/)
33. R. Damadian, M. Goldsmith, L. Minkoff, NMR in cancer: XVI. FONAR image of the live human body. *Physiol. Chem. Phys.* **9**, 97–100, 108 (1977). pmid: [90957](https://pubmed.ncbi.nlm.nih.gov/90957/)
34. W. A. Edelstein, J. M. Hutchison, G. Johnson, T. Redpath, Spin warp NMR imaging and applications to human whole-body imaging. *Phys. Med. Biol.* **25**, 751–756 (1980). doi: [10.1088/0031-9155/25/4/017](https://doi.org/10.1088/0031-9155/25/4/017); pmid: [7454767](https://pubmed.ncbi.nlm.nih.gov/7454767/)
35. J. P. Marques, F. J. J. Simonis, A. G. Webb, M. R. I. Low-field, M. R. I. Low-field, An MR physics perspective. *J. Magn. Reson. Imaging* **49**, 1528–1542 (2019). doi: [10.1002/jmri.26637](https://doi.org/10.1002/jmri.26637); pmid: [30637943](https://pubmed.ncbi.nlm.nih.gov/30637943/)
36. L. L. Wald, P. C. McDaniel, T. Witzel, J. P. Stockmann, C. Z. Cooley, Low-cost and portable MRI. *J. Magn. Reson. Imaging* **52**, 686–696 (2020). doi: [10.1002/jmri.26942](https://doi.org/10.1002/jmri.26942); pmid: [31605435](https://pubmed.ncbi.nlm.nih.gov/31605435/)
37. M. Sarracan, N. Salameh, M. R. I. Low-Field, How Low Can We Go? A Fresh View on an Old Debate. *Front. Phys.* **8**, 172 (2020). doi: [10.3389/fphy.2020.00172](https://doi.org/10.3389/fphy.2020.00172)
38. M. Dewey, T. Schink, C. F. Dewey, Claustrophobia during magnetic resonance imaging: Cohort study in over 55,000 patients. *J. Magn. Reson. Imaging* **26**, 1322–1327 (2007). doi: [10.1002/jmri.21147](https://doi.org/10.1002/jmri.21147); pmid: [17969166](https://pubmed.ncbi.nlm.nih.gov/17969166/)
39. D. M. Hudson, C. Heales, R. Meertens, Review of claustrophobia incidence in MRI: A service evaluation of current rates across a multi-centre service. *Radiography (Lond.)* **28**, 780–787 (2022). doi: [10.1016/j.radi.2022.02.010](https://doi.org/10.1016/j.radi.2022.02.010); pmid: [35279401](https://pubmed.ncbi.nlm.nih.gov/35279401/)
40. C. Jin et al., Temporary Hearing Threshold Shift in Healthy Volunteers with Hearing Protection Caused by Acoustic Noise Exposure during 3-T Multisequence MR Neuroimaging. *Radiology* **286**, 602–608 (2018). doi: [10.1148/radiol.2017161622](https://doi.org/10.1148/radiol.2017161622); pmid: [28813235](https://pubmed.ncbi.nlm.nih.gov/28813235/)
41. M. J. McJury, Acoustic Noise and Magnetic Resonance Imaging: A Narrative/Descriptive Review. *J. Magn. Reson. Imaging* **55**, 337–346 (2022). doi: [10.1002/jmri.27525](https://doi.org/10.1002/jmri.27525); pmid: [33629790](https://pubmed.ncbi.nlm.nih.gov/33629790/)
42. T. C. Arnold et al., Sensitivity of portable low-field magnetic resonance imaging for multiple sclerosis lesions. *Neuroimage Clin.* **35**, 103101 (2022). doi: [10.1016/j.nicl.2022.103101](https://doi.org/10.1016/j.nicl.2022.103101); pmid: [35792417](https://pubmed.ncbi.nlm.nih.gov/35792417/)
43. R. R. Edelman, S. Warach, Magnetic resonance imaging (2). *N. Engl. J. Med.* **328**, 785–791 (1993). doi: [10.1056/NEJM199303183281109](https://doi.org/10.1056/NEJM199303183281109); pmid: [8369029](https://pubmed.ncbi.nlm.nih.gov/8369029/)
44. R. N. Low, Abdominal MRI advances in the detection of liver tumours and characterisation. *Lancet Oncol.* **8**, 525–535 (2007). doi: [10.1016/S1470-2045\(07\)70170-5](https://doi.org/10.1016/S1470-2045(07)70170-5); pmid: [17540304](https://pubmed.ncbi.nlm.nih.gov/17540304/)
45. W. A. Curtis et al., Quantitative MRI of Diffuse Liver Disease: Current Applications and Future Directions. *Radiology* **290**, 23–30 (2019). doi: [10.1148/radiol.2018172765](https://doi.org/10.1148/radiol.2018172765); pmid: [30511906](https://pubmed.ncbi.nlm.nih.gov/30511906/)
46. A. Stabile et al., Multiparametric MRI for prostate cancer diagnosis: Current status and future directions. *Nat. Rev. Urol.* **17**, 41–61 (2020). doi: [10.1038/s41585-019-0212-4](https://doi.org/10.1038/s41585-019-0212-4); pmid: [31316185](https://pubmed.ncbi.nlm.nih.gov/31316185/)
47. T. Kamisawa, L. Wood, T. Itoi, K. Takaori, Pancreatic cancer. *Lancet* **388**, 73–85 (2016). doi: [10.1016/S0014-6736\(16\)00141-0](https://doi.org/10.1016/S0014-6736(16)00141-0); pmid: [26830752](https://pubmed.ncbi.nlm.nih.gov/26830752/)
48. K. A. Harrington, A. Shukla-Dave, R. Paudyal, R. K. G. Do, MRI of the Pancreas. *J. Magn. Reson. Imaging* **53**, 347–359 (2021). doi: [10.1002/jmri.27148](https://doi.org/10.1002/jmri.27148); pmid: [32302044](https://pubmed.ncbi.nlm.nih.gov/32302044/)
49. J. M. Llovet et al., Hepatocellular carcinoma. *Nat. Rev. Dis. Primers* **7**, 6 (2021). doi: [10.1038/s41572-020-00240-3](https://doi.org/10.1038/s41572-020-00240-3); pmid: [33479224](https://pubmed.ncbi.nlm.nih.gov/33479224/)
50. P. Gupta et al., Abbreviated MRI for hepatocellular carcinoma screening: A systematic review and meta-analysis. *J. Hepatol.* **75**, 108–119 (2021). doi: [10.1016/j.jhep.2021.01.041](https://doi.org/10.1016/j.jhep.2021.01.041); pmid: [33548385](https://pubmed.ncbi.nlm.nih.gov/33548385/)
51. R. Girardet et al., The combination of non-contrast abbreviated MRI and alpha foetoprotein has high performance for hepatocellular carcinoma screening. *Eur. Radiol.* **33**, 6929–6938 (2023). doi: [10.1007/s00330-023-09906-4](https://doi.org/10.1007/s00330-023-09906-4); pmid: [37464111](https://pubmed.ncbi.nlm.nih.gov/37464111/)
52. J. Chen et al., Early detection of nonalcoholic steatohepatitis in patients with nonalcoholic fatty liver disease by using MR elastography. *Radiology* **259**, 749–756 (2011). doi: [10.1148/radiol.11101942](https://doi.org/10.1148/radiol.11101942); pmid: [21460032](https://pubmed.ncbi.nlm.nih.gov/21460032/)
53. R. Loomba et al., Magnetic resonance elastography predicts advanced fibrosis in patients with nonalcoholic fatty liver disease: A prospective study. *Hepatology* **60**, 1920–1928 (2014). doi: [10.1002/hep.27362](https://doi.org/10.1002/hep.27362); pmid: [25103310](https://pubmed.ncbi.nlm.nih.gov/25103310/)
54. M. Yushchenko, M. Sarracan, N. Salameh, Fast acquisition of propagating waves in humans with low-field MRI: Toward accessible MR elastography. *Sci. Adv.* **8**, eab05739 (2022). doi: [10.1126/sciadv.abo5739](https://doi.org/10.1126/sciadv.abo5739); pmid: [36083901](https://pubmed.ncbi.nlm.nih.gov/36083901/)
55. A. Bashyam et al., A portable single-sided magnetic-resonance sensor for the grading of liver steatosis and fibrosis. *Nat. Biomed. Eng.* **5**, 240–251 (2021). doi: [10.1038/s41551-020-00638-0](https://doi.org/10.1038/s41551-020-00638-0); pmid: [32527853](https://pubmed.ncbi.nlm.nih.gov/32527853/)
56. K. Shan, G. Constantine, M. Sivanathan, S. D. Flamm, Role of cardiac magnetic resonance imaging in the assessment of myocardial viability. *Circulation* **109**, 1328–1334 (2004). doi: [10.1161/01.CIR.0000120294.67948.E3](https://doi.org/10.1161/01.CIR.0000120294.67948.E3); pmid: [15037539](https://pubmed.ncbi.nlm.nih.gov/15037539/)
57. M. P. Gammie, E. Schaub, C. L. Grines, S. G. Saba, State of the art: Evaluation and prognostication of myocarditis using cardiac MRI. *J. Magn. Reson. Imaging* **49**, e122–e131 (2019). doi: [10.1002/jmri.26611](https://doi.org/10.1002/jmri.26611); pmid: [30637834](https://pubmed.ncbi.nlm.nih.gov/30637834/)
58. J. S. Witt, S. A. Rosenberg, M. F. Bassetti, MRI-guided adaptive radiotherapy for liver tumours: Visualising the future. *Lancet Oncol.* **21**, e74–e82 (2020). doi: [10.1016/S1470-2045\(20\)30046-6](https://doi.org/10.1016/S1470-2045(20)30046-6); pmid: [32072028](https://pubmed.ncbi.nlm.nih.gov/32072028/)
59. S. Verma et al., The Current State of MR Imaging-targeted Biopsy Techniques for Detection of Prostate Cancer. *Radiology* **285**, 343–356 (2017). doi: [10.1148/radiol.2017161684](https://doi.org/10.1148/radiol.2017161684); pmid: [29045233](https://pubmed.ncbi.nlm.nih.gov/29045233/)
60. M. Kobayashi, A. Pascual-Leone, Transcranial magnetic stimulation in neurology. *Lancet Neurol.* **2**, 145–156 (2003). doi: [10.1016/S1474-4422\(03\)00321-1](https://doi.org/10.1016/S1474-4422(03)00321-1); pmid: [12849236](https://pubmed.ncbi.nlm.nih.gov/12849236/)
61. J. K. Krauss et al., Technology of deep brain stimulation: Current status and future directions. *Nat. Rev. Neurol.* **17**, 75–87 (2021). doi: [10.1038/s41582-020-00426-z](https://doi.org/10.1038/s41582-020-00426-z); pmid: [33244188](https://pubmed.ncbi.nlm.nih.gov/33244188/)
62. P. J. Keall et al., Integrated MRI-guided radiotherapy - opportunities and challenges. *Nat. Rev. Clin. Oncol.* **19**, 458–470 (2022). doi: [10.1038/s41571-022-00631-3](https://doi.org/10.1038/s41571-022-00631-3); pmid: [35440773](https://pubmed.ncbi.nlm.nih.gov/35440773/)
63. B. Zhu, J. Z. Liu, S. F. Cauley, B. R. Rosen, M. S. Rosen, Image reconstruction by domain-transform manifold learning. *Nature* **555**, 487–492 (2018). doi: [10.1038/nature25988](https://doi.org/10.1038/nature25988); pmid: [29565357](https://pubmed.ncbi.nlm.nih.gov/29565357/)
64. P. M. Johnson, Y. W. Lui, The deep route to low-field MRI with high potential. *Nature* **623**, 700–701 (2023). doi: [10.1038/d41586-023-03531-3](https://doi.org/10.1038/d41586-023-03531-3); pmid: [37964114](https://pubmed.ncbi.nlm.nih.gov/37964114/)
65. A. M. Coffey, M. L. Truong, E. Y. Chekmenev, Low-field MRI can be more sensitive than high-field MRI. *J. Magn. Reson.* **237**, 169–174 (2013). doi: [10.1016/j.jmr.2013.10.013](https://doi.org/10.1016/j.jmr.2013.10.013); pmid: [24239701](https://pubmed.ncbi.nlm.nih.gov/24239701/)
66. F. Resner, H. C. Seton, J. M. Hutchison, Cryogenic receive coil and low noise preamplifier for MRI at 0.01T. *J. Magn. Reson.* **203**, 57–65 (2010). doi: [10.1016/j.jmr.2009.11.021](https://doi.org/10.1016/j.jmr.2009.11.021); pmid: [20031458](https://pubmed.ncbi.nlm.nih.gov/20031458/)
67. J. D. Sánchez-Heredia et al., Autonomous cryogenic RF receive coil for ^{13}C imaging of rodents at 3 T. *Magn. Reson. Med.* **84**, 497–508 (2020). doi: [10.1002/mrm.28113](https://doi.org/10.1002/mrm.28113); pmid: [31782552](https://pubmed.ncbi.nlm.nih.gov/31782552/)
68. S. Wei et al., Optimization design of a permanent magnet used for a low field (0.2 T) movable MRI system. *Magn. Reson. Mater. Biol. Phys. Med.* **36**, 409–418 (2023). doi: [10.1007/s10334-023-01090-2](https://doi.org/10.1007/s10334-023-01090-2); pmid: [37081246](https://pubmed.ncbi.nlm.nih.gov/37081246/)
69. P. Campbell, *Permanent Magnet Materials and their Application*, P. Campbell, Ed. (Cambridge Univ. Press, 1994), chap. 3, pp. 57–81.
70. M. Sagawa, S. Fujimura, N. Togawa, H. Yamamoto, Y. Matsuuwa, New material for permanent magnets on a base of Nd and Fe (invited). *J. Appl. Phys.* **55**, 2083–2087 (1984). doi: [10.1063/1.333572](https://doi.org/10.1063/1.333572)
71. B. Gruber, M. Froeling, T. Leiner, D. W. J. Klomp, RF coils: A practical guide for nonphysicists. *J. Magn. Reson. Imaging* **48**, 590–604 (2018). doi: [10.1002/jmri.26187](https://doi.org/10.1002/jmri.26187); pmid: [29897651](https://pubmed.ncbi.nlm.nih.gov/29897651/)
72. D. P. Kingma, J. Ba, Adam: A Method for Stochastic Optimization. [arXiv:1412.6980 \[cs.LG\]](https://arxiv.org/abs/1412.6980) (2015).
73. E. M. Haacke, E. D. Lindsdorff, W. Lin, A fast, iterative, partial-fourier technique capable of local phase recovery. *Journal of Magnetic Resonance* (1969) **92**, 126–145 (1991). doi: [10.1016/0022-2364\(91\)90253-P](https://doi.org/10.1016/0022-2364(91)90253-P)
74. M. Maggioni, V. Katkovnik, K. Egiazarian, A. Foi, Nonlocal transform-domain filter for volumetric data denoising and reconstruction. *IEEE Trans. Image Process.* **22**, 119–133 (2013). doi: [10.1109/TIP.2012.2210725](https://doi.org/10.1109/TIP.2012.2210725)
75. Y. Zhang, K. Li, K. Li, L. Wang, B. Zhong, Y. Fu, Image Super-Resolution Using Very Deep Residual Channel Attention Networks. [arXiv:1807.02758 \[cs.CV\]](https://arxiv.org/abs/1807.02758) (2018).
76. O. Ronneberger, P. Fischer, T. Brox, "U-net: Convolutional networks for biomedical image segmentation" in *Medical Image Computing and Computer-Assisted Intervention-MICCAI 18th International Conference* (Springer, 2015), pp. 234–241.
77. Ö. Çiçek, A. Abdulkadir, S. S. Lienkamp, T. Brox, O. Ronneberger, "3D UNet: learning dense volumetric segmentation from sparse annotation" in *Medical Image Computing and Computer-Assisted Intervention-MICCAI 19th International Conference* (Springer, 2016), pp. 424–432.
78. T.-Y. Lin et al., "Feature pyramid networks for object detection" in *Proceedings of the IEEE conference on computer vision and pattern recognition* (IEEE, 2017), pp. 2117–2125.
79. S. Woo, J. Park, J.-Y. Lee, I. S. Kweon, CBAM: Convolutional Block Attention Module. [arXiv:1807.06521 \[cs.CV\]](https://arxiv.org/abs/1807.06521) (2018).
80. D. C. Van Essen et al., WU-Minn HCP Consortium, The WU-Minn Human Connectome Project: An overview. *Neuroimage* **80**, 62–79 (2013). doi: [10.1016/j.neuroimage.2013.05.041](https://doi.org/10.1016/j.neuroimage.2013.05.041); pmid: [23684880](https://pubmed.ncbi.nlm.nih.gov/23684880/)
81. C. G. Peterfy, E. Schneider, M. Nevitt, The osteoarthritis initiative: Report on the design rationale for the magnetic resonance imaging protocol for the knee. *Osteoarthritis Cartilage* **16**, 1433–1441 (2008). doi: [10.1016/j.joca.2008.06.016](https://doi.org/10.1016/j.joca.2008.06.016); pmid: [18786841](https://pubmed.ncbi.nlm.nih.gov/18786841/)
82. C. Cohen-Adad et al., Open-access quantitative MRI data of the spinal cord and reproducibility across participants, sites and manufacturers. *Sci. Data* **8**, 219 (2021). doi: [10.1038/s41597-021-00941-8](https://doi.org/10.1038/s41597-021-00941-8); pmid: [34400655](https://pubmed.ncbi.nlm.nih.gov/34400655/)
83. G. McGibney, M. R. Smith, S. T. Nichols, A. Crawley, Quantitative evaluation of several partial Fourier reconstruction algorithms used in MRI. *Magn. Reson. Med.* **30**, 51–59 (1993). doi: [10.1002/mrm.1910300109](https://doi.org/10.1002/mrm.1910300109); pmid: [8371675](https://pubmed.ncbi.nlm.nih.gov/8371675/)
84. Z. Wang, A. C. Bovik, H. R. Sheikh, E. P. Simoncelli, Image quality assessment: From error visibility to structural similarity. *IEEE Trans. Image Process.* **13**, 600–612 (2004). doi: [10.1109/TIP.2003.819861](https://doi.org/10.1109/TIP.2003.819861); pmid: [15376593](https://pubmed.ncbi.nlm.nih.gov/15376593/)

85. Y. Zhao *et al.*, Whole-body Magnetic Resonance Imaging at 0.05 Tesla, v1, Zenodo; <https://zenodo.org/records/10612819> (2024).

ACKNOWLEDGMENTS

We thank V. Vardhanabutti, F. Huang, G. Leung, W. Seto, L. Feng, and Y. Liu for advice and assistance; J. Zhang, J. Hu, P. Cao, X. Li, and Z. Yue for assistance; K. Wu for writing assistance; and C. Blackmore, J. Gore, P. van Zijl, J. Hennig, B. Rosen, G. Brittenham, M. Prince, Y. Wang, S. Formenti, P. Hua, P. Khong, E. Lee, M. Ng, W. Chew, L. Jiang, T. Foo, M. Rosen, T. Kimberly, K. Sheth, A. Webb, M. Lyu, F. Schick, J. Griffiths, J. Helpern, X. Zhang, H. Fujita, L. Chen, G. Teng, D. Gao, J. Guo, J. Liu, H. Xu, H. Tong, J. Zhu, S. Zhu, S. Pourrahimi, L. Wald, C. Cooley, J. Alonso, M. Sarracanie, F. Knoll, Z. Liang, T. Vaughan, S. Geethanath, H. Yang, C. Hoven, and K. Chan for inspiring discussions and

assistance. We thank Ms. S. Kwok for assistance in volunteer recruitment, and all volunteers who participated in this study.

Funding: This work was supported by Hong Kong Research Grant Council (R7003-19F, HKU1712120, HKU17127121, HKU17127022, and HKU17127523) and Lam Woo Foundation to E.X.W. **Author contributions:**

E.X.W. and Y.Z. contributed to or advised on conceptualization, design, and development. Y.Z., Y.D., V.L., C.M., S.S., L.X., A.T.L., and E.X.W. contributed to the technical development of the system and calibrations, imaging protocols, data acquisition, preparation, and processing. E.X.W. and Y.Z. wrote the manuscript. All authors contributed to reviewing the manuscript. **Competing interests:** All authors declare that they have no competing interests. **Data and materials availability:**

Primary data used, analyzed, and generated to support the findings of this study, as well as key technical design documents and custom PF-SR and deep-DSP software

code, can be accessed and downloaded from Zenodo (85).

License information: Copyright © 2024 the authors, some rights reserved; exclusive licensee American Association for the Advancement of Science. No claim to original US government works. <https://www.science.org/about/science-licenses-journal-article-reuse>

SUPPLEMENTARY MATERIALS

science.org/doi/10.1126/science.adm7168

Figs. S1 to S5

Tables S1 to S5

Movies S1 to S10

Captions for Movies S1 to S10

Submitted 3 November 2023; accepted 19 March 2024
10.1126/science.adm7168